Marine and Petroleum Geology 86 (2017) 228–247

Contents lists available at ScienceDirect

Marine and Petroleum Geology

journal homepage: www.elsevier.com/locate/marpetgeo

Research paper

Authigenic minerals from the Paola Ridge (southern Tyrrhenian Sea): Evidences of episodic methane seepage

F. Franchi [a, b, *], M. Rovere [b], F. Gamberi [b], H. Rashed [c], O. Vaselli [c, d], F. Tassi [c, d]

[a] Department of Earth and Environmental Science, Botswana International University of Science and Technology (BIUST), Private Bag 16, Plot 10071, Palapye, Botswana
[b] ISMAR-CNR, U.O.S. Bologna, Via Gobetti 101, 40129 Bologna, Italy
[c] Department of Earth Sciences, University of Florence, Via G. La Pira, 4, 50121 Florence, Italy
[d] IGG-CNR, U.O.S. Florence, Via G. La Pira, 4, 50121 Florence, Italy

ARTICLE INFO

Article history:
Received 6 March 2017
Received in revised form
10 May 2017
Accepted 21 May 2017
Available online 25 May 2017

Keywords:
Cold seep
Methanogenesis
Authigenic carbonates
Authigenic siderite
Trace elements
REE
Sulfate-methane transition zone
Stable isotopes

ABSTRACT

Paola Ridge, along the NW Calabrian margin (southern Tyrrhenian Sea), is one of the few reported deep sea sites of precipitation of authigenic carbonates in the Tyrrhenian Sea. Here, the changing composition of the seeping fluids and the dynamic nature of the seepage induced the precipitation of pyrite, siderite and other carbonate phases. The occurrence of this array of authigenic precipitates is thought to be related to fluctuation of the sulfate-methane transition zone (SMTZ).

Concretions of authigenic minerals formed in the near sub-bottom sediments of the Paola Ridge were investigated for their geochemical and isotopic composition. These concretions were collected in an area characterized by the presence of two alleged mud volcanoes and three mud diapirs. The mud diapirs are dotted by pockmarks and dissected by normal faults, and are known for having been a site of fluid seepage for at least the past 40 kyrs. Present-day venting activity occurs alongside the two alleged mud volcanoes and is dominated by CO_2-rich discharging fluids. This discover led us to question the hypothesis of the mud volcanoes and investigate the origin of the fluids in each different domed structure of the study area.

In this study, we used stable isotopes (carbon and oxygen) of carbonates coupled with rare earth element (REE) composition of different carbonate and non-carbonate phases for tracing fluid composition and early diagenesis of authigenic precipitates. The analyses on authigenic precipitates were coupled with chemical investigation of venting gas and sea-water.

Authigenic calcite/aragonite concretions, from surficial sediments on diapiric structures, have depleted ^{13}C isotopic composition and slightly positive $\delta^{18}O$ values. By contrast, siderite concretions, generally found within the first 6 m of sediments on the alleged mud volcanoes, yielded positive $\delta^{13}C$ and $\delta^{18}O$ values. The siderite REE pattern shows consistent LREE (light REE) fractionation, MREE (medium REE) enrichment and positive Gd and La anomalies. As shown by the REE distribution, the ^{13}C-depleted composition and their association with chemosymbiotic fauna, calcite/aragonite precipitated at time of moderate to high methane flux close to the seafloor, under the influence of bottom seawater. Authigenic siderite, on the other hand, formed in the subseafloor, during periods of lower gas discharges under prolonged anoxic conditions within sediments in equilibrium with ^{13}C-rich dissolved inorganic carbon (DIC) and ^{18}O-rich water, likely related to methanogenesis and intermittent venting of deep-sourced CO_2.

1. Introduction

Submarine seepage areas originate from the migration of methane-rich fluids and their discharge at the seafloor through peculiar morphologic features such as mud volcanoes (e.g., Krastel et al., 2003; Løseth et al., 2009), pockmarks (e.g., Hovland et al., 2002; Sultan et al., 2014) and mud diapirs (e.g., Rovere et al.,

* Corresponding author. Department of Earth and Environmental Science, Botswana International University of Science and Technology (BIUST), Private Bag 16, Palapye, Botswana.
E-mail address: franchif@biust.ac.bw (F. Franchi).

http://dx.doi.org/10.1016/j.marpetgeo.2017.05.031
0264-8172/

2014). In such areas, faults may act as plumbing systems, favoring the uprising of fluids from deep-seated sources, which can affect at different degrees the diagenesis of marine sediments (e.g., Hein et al., 2006). The fluids often sustain complex ecosystems with a high degree of biodiversity (e.g., Levin et al., 2016) and significant chemosynthetic biomass, which may drive anaerobic oxidation of methane (AOM) and trigger carbonate mineral precipitation (Boetius and Suess, 2004). In such environments, methane is thought to be mostly consumed by sulfate-dependent AOM mediated by microbial consortia in the sulfate-methane transition zone (SMTZ) (Boetius et al., 2000). The AOM-related processes increase bicarbonate and hydrogen sulfides. This, in turns, increases the pore water alkalinity and favors the precipitation of authigenic carbonates. It has been proved that the discontinuous seepage of methane may influence the overall geochemical composition of the authigenic carbonates affecting both stable isotope composition of carbon and oxygen (Birgel et al., 2011; Hu et al., 2014) and REE distribution (Solomon et al., 2008; Kim et al., 2012; Hu et al., 2014).

Whether cold seeps are by definition sites of active or extinct fluid escape dominated by dissolved methane, hydrothermal vents are normally considered as result of volcanic activity and characterized by higher temperatures and dominated, among the others, by dissolved CO_2 and H_2S (Joseph, 2017 and references therein). While hydrothermal vents were first discovered in 1977 along the Galápagos Rift, a spur of the East Pacific Rise (Corliss et al., 1979), the first finding of cold seeps occurred in the Gulf of Mexico (Paull et al., 1984). The term cold seep soon became popular to identify seafloor sites where hydrocarbon-rich fluids are released, and have temperatures comparable with that of the surrounding seawater. Here, we abide to the aforementioned definitions and therefore refer to sites dominated by dissolved methane as 'seeps', and sites dominated by CO_2 with the term 'vents'.

The eastern Mediterranean Sea and the eastern part of the central Mediterranean Sea have extensively been investigated for the occurrence of mud volcanism and cold seeps related to the presence of collision zones (Ceramicola et al., 2014; Lykousis et al., 2009; Mascle et al., 2014). In the western part of the central Mediterranean Sea, the Tyrrhenian Sea, evidences of fluid seepage are limited to the Adriatic Sea (Geletti et al., 2008), Strait of Sicily, Sardinian Margin (Dalla Valle and Gamberi, 2011) and Malta Plateau (Savini et al., 2009; Micallef et al., 2011; Taviani et al., 2013), mostly in the form of pockmarks, occasionally associated with methane-imprinted carbonates (Capozzi et al., 2012; Cangemi et al., 2010; Angeletti et al., 2015; Taviani et al., 2015). In the westernmost part of the Central Mediterranean Sea, the Tyrrhenian Sea, little evidence of past and present fluid circulation was found in the deep sea, except for the Paola Ridge, along the NW Calabrian margin (Fig. 1). This area, surrounded by hydrothermally active vent sites (Peters et al., 2011; Passaro et al., 2016), has been described as a site of seepage, gas venting at the seafloor and precipitation of methane-related authigenic carbonates (Gamberi and Rovere, 2010; Rovere et al., 2014, 2015).

Although authigenic calcite and aragonite have commonly been used for geochemical characterization of seeping fluids and paleoenvironmental reconstruction at recent (e.g., Himmler et al., 2010; Peckmann et al., 2001; Peckmann and Thiel, 2004; Capozzi et al., 2012; Magalhães et al., 2012) and fossil (e.g., Blumenberg et al., 2015; Cau et al., 2015; Viola et al., 2015) methane seeps, the occurrence of authigenic siderite at seepage sites is less documented (Fritz et al., 1971; Curtis et al., 1972; Mozley and Wersin, 1992; Rongemaille et al., 2011). Siderite nodules have been reported in modern settings associated with methane seepage (Niger delta; Rongemaille et al., 2011) or methane hydrate decomposition (Black Outer Ridge; Matsumoto, 1989), and with highly ferruginous, low-sulfate, anoxic lake waters (e.g., Wittkop et al., 2014). Despite the wide occurrence of sedimentary siderite little is known about the chemical conditions in which siderite forms in deep marine settings. Siderite is a common early diagenetic mineral that likely records the chemistry of the mineralizing fluids providing insights into the characteristics of the depositional environments (Mozley and Wersin, 1992). Pioneering studies of deep marine sediments, argued that the isotopic composition of siderite might be the result of the incorporation of deep circulating fluids (Clayton and Epstein, 1961; Muehlenbachs and Hodges, 1978; Cocker et al., 1982).

To characterize the pattern of fluid seepage that has triggered the precipitation of authigenic minerals at Paola Ridge, whole rock geochemistry (REE) and stable isotope (carbon and oxygen) composition were investigated. REE composition of carbonates has successfully been applied to the reconstruction of seeping fluids composition and redox conditions in both recent (e.g., Himmler et al., 2010; Hu et al., 2014) and ancient (e.g., Nothdurft et al., 2004; Feng et al., 2009; Franchi et al., 2015, 2016) settings. The variation of the REE pattern from the standard seawater composition (e.g., Zhong and Mucci, 1995; Zhang and Nozaki, 1998) is related to either mixing processes between methane-rich and hydrothermal fluids (e.g., Kamber et al., 2004; Feng et al., 2009) or modification of pore water redox conditions (Kim et al., 2012; Hu et al., 2014).

Although extensive literature deals with the characterization of authigenic precipitates at methane seeps, few cases are known where pyrite, siderite, dolomite and calcite/aragonite concretions occur in the same setting. The presence of siderite concretion alongside with pyrite concretion and the occurrence of calcite/aragonite concretions lined by dolomite crusts make the Paola Ridge an unparalleled laboratory for marine and petroleum geologists interested in the study of the interaction between mineralizing fluids and sub-bottom sediments.

Starting from the assumption that authigenic pyrite, siderite and calcite precipitate under different chemo-physical conditions, this paper aims at unraveling the dynamic processes occurring in the sub-bottom sediments of Paola Ridge (southern Tyrrhenian Sea) and provides an alternative interpretation of peculiar domed morphologies hitherto considered as mud volcanoes (Gamberi and Rovere, 2010; Rovere et al., 2014, 2015). By coupling trace elements and REE distributions and the $\delta^{13}C$ (‰ V-PDB) and $\delta^{18}O$ (‰ V-PDB) values, the source of the seeping fluids and redox condition during carbonate precipitation have been defined. This work aims at providing for the first time a detailed genetic scenario for the formation of diverse authigenic products precipitated under different chemo-physical conditions considering the dynamism at methane seepage sites. These consist of CO_2 venting, intermittent methane seepage and migration of the SMTZ for the formation of authigenic minerals along the Paola Ridge.

2. Geological setting

The Paola Ridge is a NNW-SSE 60-km-long and ca. 500-m-high anticline that confines the Paola Basin westward along the continental slope of the NW Calabrian margin (Fig. 1). The Paola Basin lies at the rear of the Calabrian Arc (inset of Fig. 1) in the upper plate of the Ionian subducting system (Faccenna et al., 2011). The Paola Basin, along with other basins along the Italian margins, originated from the extensional tectonics connected to the southeast migration of the Apennine Thrust Belt, this led to the opening of the Tyrrhenian Sea back arc basin, (see Milia et al., 2009; Gutscher et al., 2015 and references therein).

Cold seeps were first identified between 700 and 900 m water depth along the Paola Ridge with the aid of full-ocean depth multibeam and backscatter data (Gamberi and Rovere, 2010). The cold seeps are located on 2 structures initially defined as mud volcanoes

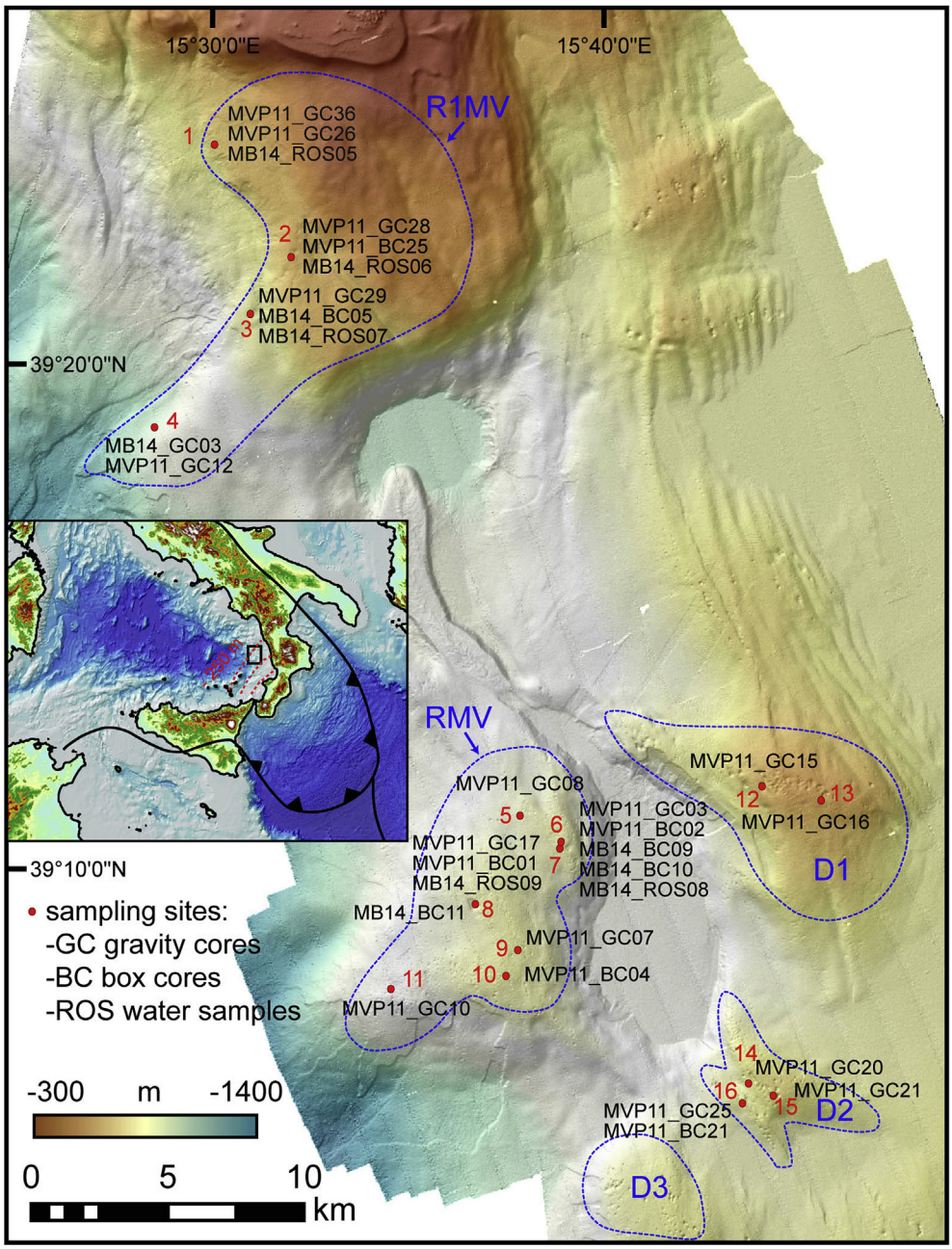

Fig. 1. Bathymetry of the Paola Ridge area. The dotted blue lines outline the pockmark-punctuated mud diapirs (D1, D2 and D3) and the alleged mud volcanoes R1MV and RMV (Rovere et al., 2014). See Table 1 for samples description. Inset: subduction system of the central Mediterranean area with location and depth of the subduction slab projected over the study area (box). (For interpretation of the references to colour in this figure legend, the reader is referred to the web version of this article.)

(RMV and R1MV structures; Gamberi and Rovere, 2010; Rovere et al., 2014) and 3 main mud diapirs (D1, D2, D3), characterized by the presence of large fields of pockmarks (Fig. 1).

Higher resolution geophysical data acquisitions and seafloor sampling campaigns were carried out in 2011 and 2014 (Rovere et al., 2014). During these campaigns active gas venting at the seafloor, gas plumes in the water column and precipitation of Fe-Mn-oxy-hydroxides, sulfide and siderite in the sub-seafloor of the mud volcanoes were detected (Rovere et al., 2014, 2015). Authigenic calcite and aragonite concretions were found in the near sub-bottom sediments on the mud diapirs. These carbonates are associated with chemosymbiotic bivalves, whose radiocarbon indicated ages from a few centuries to at least the past 40 kyrs (Rovere et al., 2015).

All the structures in the area are confined and controlled by normal faults, which represent the offshore prolongation of the fault zones dissecting the Calabrian Arc on land and are thought to play a key role in driving the fluid seepage, especially in the diapirs D1 and D2 (Rovere et al., 2014).

3. Materials and methods

Bathymetry, seafloor backscatter and seismic data, gravity- and box-coring samples were acquired in the Paola Ridge area aboard the R/V Urania in 2011 and 2014 (Rovere et al., 2014, 2015). Whole core magnetic susceptibility profiles were obtained by means of a

Bartington MS2 meter coupled with a MS2C core-logging sensor at 2 cm spacing.

3.1. Core description

The schematic logs of all the sampled cores are shown in Fig. 2. The sediment cores GC03 and GC17 were sampled at water depths of respectively 550 and 725 m in venting sites of the RMV structure (Fig. 1). GC28 was sampled at a venting site on the R1MV structure. The sediments were deformed and disrupted by gas expansion in the core barrel during the recovering of the coring device. Sulfide and siderite samples were present at different depths (Fig. 2). The sediment cores GC12 (1055 m water depth), GC26 (579 m water depth) and GC29 (707 m water depth) were collected on the R1MV structure (Fig. 1), where gas was apparently trapped 2–3 m below the seafloor. Degassing slowly started when the cored samples were already stored on the deck of the ship, resulting in the formation of expansion cracks (Fig. 2). The core GC12 was collected in the lower slope of the R1MV structure. The cores GC07, GC08 and GC10 were collected on the top of the RMV structure (Fig. 1) and showed features similar to the previously described expansion cracks. They were collected from sites of either slow gas venting or where gas was trapped below the seafloor. The core GC10 was collected at 870 m water depth, in the lower slope of the RMV structure, similarly to GC12, where seismic transparent bodies, interpreted as mudflows, trap the gas a few meters below the seafloor (cf. Rovere et al., 2014). The cores GC15 and GC16 were sampled on the D1 diapir at 520–550 m water depth (Fig. 1). The GC15 core penetrated the sediment down to a depth of 4.27 m, whilst the core barrel of GC16 captured some carbonate concretions at the seafloor (Cal-C, Cal-N; Fig. 2). Core GC15 was characterized by evidence of past intense bioturbation and frequent shell fragments of bivalve mollusks typical of reducing environments, associated with abundant decapod claws (Fig. 2). The cores GC20, GC21 and GC25 were collected between 653 and 694 m water depth across a fault scarp that dissect the D2 diapir (Fig. 1). Core GC20 impacted against a 10-cm-thick aragonite substrate located 1 m below the seafloor. Aragonite was associated with chemosymbiotic bivalves (cf. Rovere et al., 2014, 2015) and abundant remnants of the decapod *Calliax* sp. (Fig. 2). Core GC25 also impacted an aragonite crust, which was located 1 m below the seafloor and associated with chemosymbiotic bivalves. The box core BC25, collected in the same sampling station of core GC25, contained aragonite with vuggy and spongy fabric (Cal-H, Table 1). Core GC21 penetrated in the sediment for 4.4 m. Bioturbation and abundant fragments of chemosymbiotic bivalves were observed throughout the sediment succession. An aragonite crust was found in the coring samples, between 2 m and 2.40 m below the seafloor (Fig. 2).

From 16 sampling stations at 16 different sites (Figs. 1–2, Table 1), a total of 32 samples of mud and 37 concretions were collected and analyzed for mineralogical and chemical composition (Tables 2–6). Twenty-one samples are carbonates of different composition: aragonite, calcite, dolomite and siderite (Table 1). For the sake of clarity, the samples were divided into five groups: i) calcite/aragonite concretions (Table 2), ii) siderite concretions (Table 3), iii) sulfide concretions (Table 4), iv) Fe-oxy-hydroxide concretions (Table 5) and v) muddy sediments (Table 6). The petrographic- and microfacies-based analyses were performed using standard petrographic thin sections at Istituto di Scienze Marine-Consiglio Nazionale delle Ricerche (ISMAR-CNR) and Earth and Environmental Science Department at Botswana International University of Science and Technology (BIUST).

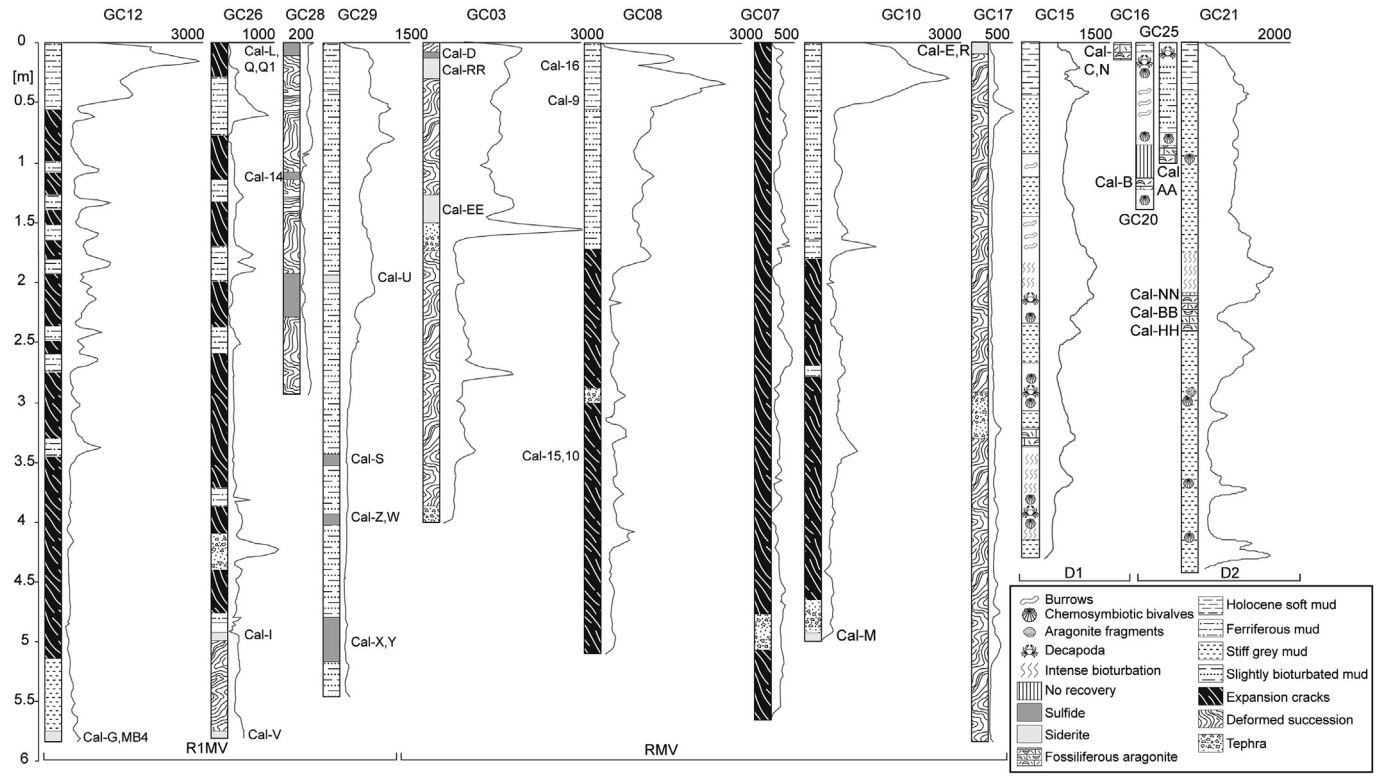

Fig. 2. Simplified lithostratigraphy and magnetic susceptibility of the drill cores from which all the carbonate, sulfide, Fe-oxy-hydroxide and mud samples were collected for this study. Magnetic susceptibility is in S.I. x 10^6. Some of the samples, listed in Table 1, are also outlined along the core logs. All the cores displayed in the figure were collected during the MVP11 cruise.

3.2. Gas and water samples

Since strong degassing was noticed once cores were brought to the surface, gases from the discharging vents were collected from the R1MV (MB14_BC05, Fig. 1; Table 7) and the RVM structures (MB14_BC09, Fig. 1; Table 7). The gas samples ware then transferred into a 250 mL pre-evacuated glass flask by using a silicon tube inserted into the water vent for major components and $\delta^{13}C$-CO_2 (see methods in Vaselli et al., 2006).

Five seawater samples (Table 8) were collected at the interface with the sea bottom by means of a rosette sampler alongside R1MV (MB14_ROS5, MB14_ROS6 and MB14_ROS7) and RMV (MB14_ROS8 and MB14_ROS9). Once retrieved at the surface, each water sample was divided into two aliquots and both filtered at 0.45 ŧm. The first one was transferred to a 125 mL plastic bottle for the determination of the main anions while the second one was acidified with 0.5 mL of suprapur HCl in a 50 mL plastic bottle for the analysis of the main cations. Eventually, a third aliquot was transferred to pre-weighed 100 mL glass bottles, where 5 mL of a 1M Na_2CO_3 solution were previously added, for the determination of free-CO_2. Sampling procedures followed the protocol described in Cabassi et al. (2011).

3.3. Analytical procedure

Bulk mineralogy was analyzed by X-ray diffraction on powdered samples using a Philips PW 1050/37 diffractometer, with a Cu anode (40 kV accelerating voltage and 20 mA current), a graphite monochromator and the X'Pert PRO Philips acquisition system (detection limit 4%). The analyses were carried out with a goniometry speed of 2θ°/min, in a scanning range 5–70 2θ° for the rock samples and 2-32 2θ° for the clay fraction.

Sub-samples for geochemical analyses were powdered using a planetary mill equipped with 4 grinding agate bowls. Major and trace elements (Tables 2–6, supplementary materials S1) were analyzed by X-ray fluorescence (XRF), using a Rigaku II wavelength dispersive spectrometer with a Rh anode on pressed pellets of bulk sample powder, and inductively coupled plasma - mass spectrometry (ICP-MS) at the ACME Laboratories (Canada). Seven additional samples of siderite were analyzed at Activation Laboratories LTD (Canada). In the first set of analyses the powdered samples, weighed (about 0.2 g) in PTFE tubes, were dissolved with the three-acid (HCl-HF-HNO_3) dissolution method, in a microwave oven. From each sample, an aliquot of approximately 5mL was then transferred to 10 mL tubes and placed in an automatic sampler and analyzed with an Agilent 700 Series ICP-MS. In the second set of analyses (Table 3) the fusion procedure followed the lithium metaborate/tetraborate protocol developed by Activation Laboratories (code 4B and 4B2; see http://www.actlabs.com/). Samples were mixed with a flux of lithium metaborate and lithium tetraborate and fused in an induction furnace. The molten melt was immediately poured into a solution of 5% nitric acid containing an internal standard, and mixed continuously until completely dissolved. Each batch of samples contained a method reagent blank, a certified reference material and 17% replicates. The samples were then investigated for their trace elements and REE composition using a Perkin Elmer Sciex ELAN 6000, 6100 or 9000 ICP-MS. Three blanks and five controls (three before each sample group and two after) were analyzed during each batch of samples. Duplicates were fused and analyzed every 15 samples (instrument was recalibrated every 40 samples). Accuracy for trace element determinations was ca. 5% for element concentrations >10 ppm and 10–15% for lower concentrations. Detection limits for XRF and ICP-MS analysis were ca. 3 and 0.1 ppm, respectively.

The relative abundances of REE were normalized to the Post Archean Average Australian Shale (PAAS, Taylor and McLennan, 1985), representing the estimated average terrigenous input to the oceanic environment. We calculated ΣREE, Y/Ho, Ce, Eu and Gd anomalies (Tables 2–6) and the relation between these proxies and trace and transition elements for the studied samples. Light REE (LREE) fractionation was calculated as Pr_{SN}/Yb_{SN} to avoid bias due to anomalous La and Ce concentrations. Medium REE (MREE) enrichment was calculated as Gd_{SN}/Yb_{SN}. Normalized Ce, Eu and Gd anomalies were calculated using the geometric equation given by Lawrence et al. (2006):

$$(Ce/Ce^*)_{SN} = Ce_{SN} / [Pr_{SN} * (Pr_{SN} / Nd_{SN})] \quad (1)$$

$$(Eu/Eu^*)_{SN} = [Eu_{SN} / [(Sm_{SN})^2 * Tb_{SN}]^{1/3} \quad (2)$$

$$Gd/Gd^* = [Gd_{SN} / [(Tb_{SN})^2 * Sm_{SN}]^{1/3} \quad (3)$$

Stable isotopes (C and O) measurements were performed on powdered samples and were carried out using the Finnigan Delta S mass spectrometer at the Department of Physical and Geological Sciences of the University of Parma (Italy). Prior the analysis the powdered samples were ignited under vacuum at 550 °C to remove all organic matter. Then the samples were transferred to 25 mL flasks equipped with a glass tap and reacted with 4 mL of 100% anhydrous phosphoric acid at 25 °C after degassing H_3PO_4 under vacuum. The samples were successively treated for selective acid extraction (see protocol in Al-Aasm et al., 1990). The results were reported in the conventional δ‰ notation against the V-PDB (Vienna Pee Dee Belemnite) standard with a reproducibility of ±0.3‰. Standards used for estimation of external precision were Carrara and San Vincenzo marbles (Internal), NBS18 and 327 NBS19 (International), whereas the analytical error and the reproducibility were ±0.05‰ and ±0.1‰, respectively (see Vaselli et al., 2006).

Inorganic low-solubility gases (Table 7) were analyzed by gas-chromatography (GC) using a Shimadzu 15A equipped with a 10 m long 5A-molecular sieve column and a thermal conductivity detector (TCD). Methane was analyzed using a Shimadzu 14A gas chromatograph equipped with a 10-m-long stainless steel column packed with Chromosorb PAW 80/100 mesh coated with 23% SP 1700 and a flame ionization detector (FID) following the protocol described in Passaro et al. (2016).

The seawater samples (Table 8) were analyzed at the Department of Earth Sciences of the University of Florence by cation- (Na^+, K^+, Ca^{2+}, Mg^{2+}, Li^+, and NH^{4+}) and anion- (Cl^-, SO_4^{2-}, NO^{3-}, Br^- and F^-) chromatography by using Metrohm 861 and 761 ion-chromatographers, following the protocol in Cabassi et al. (2011).

4. Results

4.1. Petrography of the concretions

4.1.1. Calcite/aragonite concretions

Calcite/aragonite concretions, collected from different depths (Table 1), are only found in cores located on D1 and D2 structures (Fig. 2). The concretions are a few centimeters across, showing variable degree of lithification from poorly cemented to more lithified types (Fig. 3A). These concretions are mainly mudstone/wackestone with foraminifera remnants cemented by mottled to homogeneous micrite (Fig. 4A). Patches of sandy limestone were also observed. Porosity is generally low and vugs are filled with sparry calcite and less abundant fibrous cements. The concretions are mainly composed of aragonite with subordinate calcite and abundant terrigenous components (Table 1; Fig. 4A). Dolomite occurs as patchy cements within vugs or as millimeter-thick crusts lining the concretions. Two concretions (Cal-B and Cal-AA) consist of calcite and dolomite cemented shells of chemosymbiotic

Table 1
Sampling stations (Fig. 1), depth and description of the samples (sediments, concretions, water and gas). Mineralogical and stable isotope composition of limestone and siderite samples is also provided. Data from Rovere et al. (2015) are highlighted in gray.

Site	Sampling Station	Sample	Mineralogy				$\delta^{13}C$ (‰)	$\delta^{18}O$ (‰)	Depth below seafloor (m)	Water depth (m)	Structure
			Calcite (vol%)	Dolomite (vol%)	Aragonite (vol%)	Other					
1	MB14_ROS05	Water							0	579	R1MV
	MVP11_GC36	Cal-V	–	–	–	Siderite (ter.)	10.4	9.5	6		
	MVP11_GC26	Cal-T	–	–	–	Goethite			0.5		
		Cal-I	–	–	–	Siderite (Qz)	10.6	9.2	5		
2	MB14_ROS06	Water							0	549	
	MVP11_BC25	Cal-L	–	–	–	Pyrite			0.5		
		Cal-Q	–	–	–	Pyrite			0.5		
		Cal-Q1	–	–	–	Sulfur			0.5		
	MVP11_GC28	Cal-20	–	–	–	Siliciclastic			0.3		
		Cal-21	–	–	–	Siliciclastic			0.8		
		Cal-4	Trace	–	–	Siliciclastic			0.9		
		Cal-14	–	–	–	Pyrite			1.1		
		Cal-18	–	–	–	Hematite			1.4		
		Cal-12	–	–	–	Hematite			1.8		
3	MB14_ROS07	Water							0	707	
	MVP11_GC29	Cal-U	–	–	–	Siderite (ter.)	10.3	9.3	2		
		Cal-S	–	–	–	Pyrite			3.5		
		Cal-Z	–	–	–	Pyrite			4		
		Cal-W	–	–	–	Pyrite			4.1		
		Cal-X	–	–	–	Pyrite			5		
		Cal-Y	–	–	–	Pyrite			5		
	MB14_BC05	Gas							0		
4	MVP11_GC12	Cal-G	–	–	–	Siderite (Qz)	8.4	9.5	6	1055	
	MB14_GC03	Cal-MB4	–	–	–	Siderite (Qz)			6.2		
5	MVP11_GC08	Cal-16	Trace			Siliciclastic			0.3	760	RMV
		Cal-9	Trace			Siliciclastic			0.7		
		Cal-15	Trace			Siliciclastic			3.6		
		Cal-10	Trace			Siliciclastic			3.7		
6	MB14_ROS08	Water							0	726	
	MVP11_BC02	Cal-D	–	–	–	Pyrite			0.2		
	MB14_BC09	Gas							0		
	MVP11_GC03	Cal-RR	–	–	–	Siderite (Qz)	8.7	9.3	0.3		
		Cal-31	–	–	–	Siliciclastic			0.4		
		Cal-EE	–	–	–	Siderite (Qz)	9.1	9.1	1.3		
		Cal-28	–	–	–	Siliciclastic			2.1		
7	MB14_ROS09	Water							0	728	
	MVP11_GC17	Cal-E	–	–	–	Siderite (ter.)	8.3	9.6	0–1		
		Cal-R	Trace			Siderite (ter.)	7.7	9.9	0–1		
		Cal-7	–	–	–	Siliciclastic			0–1		
		Cal-8	–	–	–	Siliciclastic			0–1		
		Cal-1	–	–	–	Hematite			1.3		
		Cal-2	–	–	–	Siliciclastic			3.2		
		Cal-19	–	–	–	Siliciclastic			4		
		Cal-6	Trace			Siliciclastic			4.8		
		Cal-23	–	–	–	Siliciclastic			5.3		
		Cal-A	–	–	–	Siderite (Qz)	8.7	8.7	6		
	MVP11_BC01	Cal-K	–	–	–	Pyrite			0.5		
		Cal-O	–	–	–	Pyrite			0.5		
8	MB14_BC11	Water							0	755	
9	MVP11_GC07	Cal-24	–	–	–	Siliciclastic			0.5	709	
		Cal-5	–	–	–	Siliciclastic			1.5		
		Cal-13	–	–	–	Siliciclastic			2.5		
		Cal-26	–	–	–	Siliciclastic			3.5		
		Cal-3	–	–	–	Siliciclastic			3.8		
		Cal-25	–	–	–	Siliciclastic			4.7		
		Cal-11	–	–	–	Hematite			5.5		
10	MVP11_BC04	Cal-P	–	–	–	Goethite			0.5	728	
		Cal-F	–	–	–	Goethite			0.5		
11	MVP11_GC10	Cal-M	–	–	–	Siderite (Qz)	−3.2	8.8	5	870	
12	MVP11_GC15	Cal-27	Trace	–	–	Siliciclastic			3.6	557	D1
		Cal-30	Trace	–	–	Siliciclastic			3.7		
13	MVP11_GC16	Cal-N	27.0	1.7	38.3		−35.8	4.7	0	521	
		Cal-N*	0.0	100.0	0.0		−9.9	1.4	0		
		Cal-C	35.2	2.8	29.5		−35.4	5.5	0		
		Cal-C*	0.0	100.0	0.0		−23.8	5.0	0		
14	MVP11_GC20	Cal-17	Trace			Siliciclastic			0.2	653	D2
		Cal-B	17.1	1.8	48.8		−39.3	4.3	1		
		Cal-B*	0.0	100.0	0.0		−33.4	4.6	1		
15	MVP11_GC21	Cal-CC	12.2	0.0	45.5		−44.2	5.0	2	634	
		Cal-29	Trace	–	–	Siliciclastic			2.06		

(*continued on next page*)

Table 1 (*continued*)

Site	Sampling Station	Sample	Mineralogy				$\delta^{13}C$ (‰)	$\delta^{18}O$ (‰)	Depth below seafloor (m)	Water depth (m)	Structure
			Calcite (vol%)	Dolomite (vol%)	Aragonite (vol%)	Other					
		Cal-NN	14.9	0.0	53.8		−43.7	5.1	2.3		
		Cal-BB	12.9	0.0	49.9		−45.4	4.9	2.5		
		Cal-HH	10.7	0.0	53.9		−48.8	4.5	3		
		Cal-32	Trace	–	–	Siliciclastic			3.05		
16	MVP11_BC21	Cal-H	23.0	0.3	46.2		−26.3	2.8	0.5	694	
	MVP11_GC25	Cal-AA	10.5	0.0	69.9		−40.7	3.3	0.95		

* External dolomitic crusts.
Ter.: quartz, feldspar and mica.
Qz: quartz.

Table 2
Major oxides (wt. %) and trace elements (ppm) composition of calcite/aragonite concretions from the Paola Ridge.

Sample	Cal-B	Cal-C	Cal-N	Cal-H	Cal-BB	Cal-CC	Cal-AA	Cal-NN	Cal-HH
Na_2O	0.38	0.43	0.45	0.54	0.56	0.81	0.58	0.48	0.48
MgO	2.73	3.27	3.00	1.93	2.05	1.80	2.03	1.47	2.13
Al_2O_3	5.74	5.07	7.20	5.56	7.44	7.79	4.40	5.87	8.51
SiO_2	14.87	12.73	18.80	13.57	19.67	21.22	10.73	15.72	21.29
P_2O_5	0.08	0.11	0.20	0.12	0.10	0.12	0.07	0.09	0.08
K_2O	1.14	0.92	1.45	1.00	1.45	1.53	0.79	1.13	1.57
CaO	39.65	39.73	34.73	41.15	36.37	29.42	43.16	40.52	30.39
TiO_2	0.35	0.29	0.46	0.29	0.49	0.43	0.28	0.28	0.48
MnO	0.06	0.10	0.06	0.03	0.05	0.06	0.04	0.05	0.06
Fe_2O_3	3.05	3.09	4.84	2.17	3.28	3.24	2.34	2.70	3.65
L.O.I	31.04	33.76	27.90	32.66	26.97	32.11	34.40	30.63	29.34
TOT	99.08	99.50	99.08	99.02	98.42	98.52	98.83	98.94	97.98
La	19.0	18.8	21.6	22.2	16.2	23.0	13.6	14.5	21.2
Ce	36.5	37.7	43.1	42.6	31.7	45.3	26.3	28.2	40.3
Pr	3.9	3.9	4.5	4.5	3.6	5.0	2.9	3.1	4.4
Nd	14.7	14.9	17.6	15.5	13.7	19.2	10.6	11.6	16.6
Sm	2.7	2.8	3.1	3.1	2.6	3.7	2.0	2.2	3.3
Eu	0.6	0.6	0.7	0.6	0.5	0.9	0.4	0.5	0.7
Gd	2.2	2.3	3.0	2.7	2.3	3.3	1.5	2.1	2.8
Tb	0.4	0.4	0.4	0.4	0.3	0.5	0.2	0.3	0.4
Dy	2.0	1.9	2.1	2.1	2.0	2.7	1.3	1.7	2.4
Ho	0.4	0.4	0.5	0.5	0.4	0.5	0.2	0.4	0.5
Er	1.2	1.2	1.0	1.3	1.1	1.6	0.7	1.0	1.3
Tm	0.2	0.2	0.2	0.2	0.2	0.2	0.1	0.2	0.2
Yb	1.1	0.9	1.4	1.2	1.2	1.5	0.8	1.0	1.3
Lu	0.2	0.2	0.2	0.2	0.2	0.2	0.1	0.2	0.2
∑REE	85.0	86.0	99.4	97.2	76.0	107.6	60.7	67.0	95.6
Y/Ho	25.9	25.7	26.1	25.3	27.5	32.0	45.0	27.5	28.0
Ce/Ce*	1.04	1.05	1.08	0.93	0.98	1.01	0.98	0.96	0.99
Eu/Eu*	1.18	1.04	1.11	1.06	1.13	1.20	1.20	1.20	1.11
Gd/Gd*	1.00	0.98	1.13	1.06	1.19	1.08	1.11	1.15	1.11
Pr_{SN}/Yb_{SN}	1.13	1.35	1.00	1.19	0.95	1.06	1.15	1.00	1.09

bivalves (Table 1; Fig. 2).

4.1.2. Siderite concretions

Siderite concretions are only found in cores from the gas venting structures R1MV and RMV (Fig. 2). Siderite crusts and small tubular concretions (Fig. 3B–D) are embedded within the muddy sediments. The tubular concretions are normally a few centimeters long and less than 2 cm wide (Fig. 3C–D). In thin section, the concretions display a concentric zonation due to alternating reddish and dark brownish bands (Figs. 3C and 4B). These concretions are made up of dominant siderite with subordinate calcite and terrigenous minerals (quartz, muscovite, plagioclase, etc.). Most of the concretions consist of microcrystalline siderite, locally showing a clotted fabric. The terrigenous particles are mostly silt-sized and poorly sorted while the clasts of quartz are angular to sub-rounded. Generally the outer part of the tubular concretion appears turbid with a mottled fabric (Fig. 4B). Thin crusts of sulfides lined the inner part of the tubular concretion (Fig. 4B).

Two samples of siderite (Cal-FF and Cal-E) are coarse-grained, composed of coarse crystalline siderite with an equigranular hypidiotopic to xenotopic fabric (Fig. 4C).

4.1.3. Sulfide and Fe-Mn-oxy-hydroxide concretions

Sulfide concretions are dominated by pyrite and marcasite. Concretions of native sulfur were also observed (Rovere et al., 2015). They have high porosity and are typically a few centimeters across (Fig. 5). The sulfide form either isopachous crusts (Fig. 6A) or aggregates of anhedral and granular pyrite around small and coarse terrigenous clasts (Fig. 6B and C).

The Fe-Mn-oxy-hydroxide concretions are mostly made up of microcrystalline hematite with minor amount of goethite. Terrigenous material was ubiquitous and likely dominant in the bulk rock.

Table 3
Major oxides (wt. %) and trace elements (ppm) composition of siderites from the Paola Ridge. In gray, the chemical composition measured in a second laboratory (see text for further explanations).

Sample	Cal-I	Cal-G	Cal-M	Cal-E	Cal-R	Cal-A	Cal-V	Cal-U	Cal-EE	Cal-RR	Cal-I	Cal-G	Cal-M	Cal-E	Cal-RR	Cal-FF	Cal-MB4
Na_2O	0.59	0.31	0.29	0.78	0.56	0.42	0.47	2.32	0.81	0.54	0.40	0.34	0.39	0.76	0.61	0.66	0.70
MgO	1.29	1.98	2.11	1.44	1.01	0.73	0.98	1.16	1.20	1.25	0.93	2.02	1.96	0.93	0.87	0.71	1.93
Al_2O_3	7.93	2.21	3.27	9.66	5.66	4.30	4.02	4.10	9.03	6.57	2.65	1.85	2.14	5.02	3.89	4.76	4.41
SiO_2	18.78	5.52	8.75	22.64	12.89	12.38	9.80	10.23	21.75	15.38	7.38	5.23	6.23	14.29	11.44	12.72	12.22
P_2O_5	0.20	0.36	0.46	0.26	0.27	0.26	0.14	0.14	0.25	0.28	0.17	0.40	0.41	0.31	0.30	0.26	0.46
K_2O	0.96	0.33	0.52	0.09	0.67	0.52	0.55	0.68	1.25	0.84	0.19	0.29	0.35	0.78	0.65	0.80	0.67
CaO	2.89	3.59	3.32	1.10	3.04	1.52	5.56	3.41	2.63	3.77	6.29	3.35	2.76	2.71	3.55	2.02	3.49
TiO_2	0.27	0.12	0.16	0.31	0.18	0.16	0.19	0.18	0.28	0.23	0.15	0.10	0.14	0.26	0.20	0.20	0.24
MnO	0.61	1.64	0.94	0.53	0.89	0.68	1.28	0.83	0.49	0.32	1.45	1.43	1.17	0.49	0.42	0.68	1.38
Fe_2O_3	36.85	53.33	53.01	37.24	47.12	44.79	48.65	48.22	36.23	46.87	50.48	53.71	53.94	48.51	50.13	51.78	46.37
L.O.I	28.77	30.36	26.87	22.74	26.98	33.65	27.92	26.18	25.26	23.38	30.31	31.22	30.40	26.56	27.63	25.95	28.59
TOT	99.15	99.75	99.69	96.78	99.24	99.41	99.56	97.43	99.19	99.42	100.40	99.94	99.89	100.60	99.68	100.50	100.40
La	16.9	10.7	8.2	16.7	21.5	9.7	13.7	18.1	12.4	22.0	15.1	8.3	7.9	15.8	13.4	22.6	24.7
Ce	31.8	18.0	18.0	33.0	43.0	18.0	24.0	36.0	24.8	52.7	27.6	14.1	15.3	32.0	27.3	52.1	55.8
Pr	3.2	1.9	2.0	4.0	5.1	1.9	2.5	4.0	2.9	4.7	3.1	1.5	1.8	3.7	3.3	5.6	6.4
Nd	14.6	7.5	9.1	17.3	22.9	6.9	10.2	15.4	12.2	19.2	12.0	5.4	6.9	15.5	13.7	24.1	26.6
Sm	2.6	1.6	1.9	4.6	5.7	1.8	2.2	3.6	3.2	4.1	2.7	1.0	1.6	3.8	3.6	5.5	6.4
Eu	0.6	0.4	0.4	1.1	1.6	0.4	0.5	0.8	0.8	1.0	0.6	0.2	0.4	1.0	0.9	1.4	1.6
Gd	3.2	1.8	2.2	5.6	8.5	2.5	2.8	3.6	3.9	4.7	3.2	0.9	2.0	4.7	4.0	6.5	8.4
Tb	0.6	0.3	0.4	1.0	1.4	0.4	0.5	0.6	0.7	0.8	0.5	0.1	0.3	0.8	0.7	1.0	1.3
Dy	3.2	1.4	2.5	5.7	7.9	2.6	3.0	3.6	4.2	4.4	3.2	0.8	2.1	4.9	4.3	6.4	8.3
Ho	0.8	0.4	0.6	1.3	1.9	0.6	0.7	0.7	0.8	0.9	0.7	0.2	0.5	1.0	0.9	1.3	1.9
Er	2.5	1.0	2.0	3.6	5.6	1.9	2.1	2.1	2.4	2.6	2.1	0.5	1.6	2.8	2.5	3.7	5.7
Tm	0.4	0.1	0.3	0.5	0.7	0.3	0.3	0.3	0.4	0.4	0.3	0.1	0.2	0.4	0.4	0.5	0.8
Yb	2.2	0.9	1.7	3.4	4.6	1.9	2.0	2.0	2.5	2.5	2.2	0.4	1.5	2.5	2.4	3.2	5.2
Lu	0.4	0.2	0.3	0.5	0.7	0.3	0.3	0.3	0.3	0.4	0.4	0.1	0.3	0.4	0.4	0.5	0.8
∑REE	82.7	46.0	49.6	98.2	131.0	49.2	64.9	91.1	71.5	120.3	73.7	33.5	42.3	89.4	77.7	134.4	153.9
Y/Ho	35.4	35.1	38.4	30.2	30.2	25.6	37.1	31.4	32.5	32.2	40.0	30.0	50.0	35.0	40.0	33.8	45.3
Ce/Ce*	1.3	1.1	1.2	1.0	1.1	1.0	1.1	1.0	1.1	1.3	1.0	1.0	1.0	1.0	1.0	1.2	1.1
Eu/Eu*	1.0	1.1	0.9	1.1	1.2	1.0	1.1	1.1	1.1	1.1	1.1	1.4	1.1	1.2	1.2	1.2	1.1
Gd/Gd*	1.1	1.2	1.1	1.1	1.2	1.1	1.1	1.1	1.1	1.1	1.2	1.3	1.2	1.1	1.1	1.2	1.2
Pr_{SN}/Yb_{SN}	0.5	0.7	0.4	0.4	0.4	0.3	0.4	0.6	0.4	0.6	0.4	1.2	0.4	0.5	0.4	0.6	0.4

4.1.4. Muddy sediments

These sediments are vuggy to cohesive, gray to brownish mud and sandy mud. Quartz is the main component while feldspar (albite and microcline) and other silicates (muscovite, illite, kaolinite) are subordinate. Mud is mostly deformed, dissected by fractures and locally present trace of bioturbation (Fig. 2).

4.2. Stable isotopes

The studied carbonates show a relatively wide range of carbon and oxygen isotopic composition (Table 1; Fig. 7). The $\delta^{13}C$ and $\delta^{18}O$ values of calcite/aragonite concretions varied from −48.8‰ to −26.3‰ V-PDB and from 1.4‰ to 5.5‰ V-PDB, respectively (Table 1; Fig. 7). Crusts of dolomite (Cal-B, Cal-C and Cal-N) yielded $\delta^{13}C$ values ranging between −33.4‰ and −9.9‰ V-PDB. The siderite concretions yielded $\delta^{13}C$ values ranging between −3.2‰ and 10.6‰ V-PDB while $\delta^{18}O$ values were comprised between 8.7‰ (Cal-A) to 9.9‰ (Cal-R) V-PDB (Table 1; Fig. 7).

The sulfur isotopic compositions of one pyrite concretion and one native sulfur concretion were −32.7‰ and −15.3‰ V-CDT, respectively.

4.3. Major and trace elements

Major element concentrations of calcite/aragonite, siderite, sulfide, Fe-Mn-oxy-hydroxide and mud samples are reported in Tables 2–6 while trace element contents are listed in the supplementary material (S1).

Calcite/aragonite concretions were characterized by high CaO (up to 43.16 wt%) and relatively high SiO_2 contents (average 16.51 wt%; Table 2). Iron content (as Fe_2O_3) was generally lower than 5 wt% within calcite/aragonite concretions (Table 2). Siderite samples showed high Fe contents (between 36.23% and 53.94%) and average SiO_2 contents of 12.21 wt% (Table 3). Averaged CaO and MgO contents of the siderite concretions were 3.24 wt% and 1.32 wt %, respectively (Table 3). The average SiO_2 content in sulfide concretions was about 16.55 wt% (Table 4), whereas Fe-Mn-oxy-hydroxides showed higher SiO_2 contents (up to 36.12 wt%). The relatively low MnO contents (average 0.17 wt%; Table 5) of the Fe-Mn-oxy-hydroxides suggest that the concretions were mainly Fe-oxy-hydroxides. SiO_2 (average 37.66 wt%), Al_2O_3 (average 14.62 wt%) and Fe_2O_3 (average 6.97 wt%) dominated the muddy sediments whilst the CaO average content was 4.95 wt% (Table 6).

The distribution of redox-sensitive trace elements, namely U and Mo, has been investigated (Supplementary Materials, S1). Calcite/aragonite concretions show consistent concentrations of U ranging between 5.3 and 28.5 ppm. The Mo contents in the calcite/aragonite concretions are highly variable with values between 0.9 and 56 ppm. Siderite concretions yielded U values ranging between 0.4 and 13.5 ppm. Even the siderite concretions displayed highly variable Mo concentrations ranging between 1.1 and 84 ppm. Relatively large concentrations ranges of U and Mo were also showed by sulfide (0.8–12.6 ppm and 11–254.2 ppm, respectively), Fe-oxy-hydroxide (9.2 ppm and 62.7 ppm, respectively) and mud (2.6–13.3 ppm and 0.7–77.8 ppm, respectively) samples.

4.4. REE patterns

REE concentrations of calcite/aragonite, siderite, sulfides, Fe-oxy-hydroxide concretions and muddy sediments are reported in Tables 2–6 PAAS-normalized REE patterns are plotted in Figs. 8 and 9. The average REE patterns within the investigated samples vary according to the different lithotypes.

Total REE contents in the limestone samples range between 60.7

Table 4
Major oxides (wt. %) and trace elements (ppm) composition of sulfides from the Paola Ridge.

Sample	Cal-D	Cal-O	Cal-L	Cal-Q	Cal-S	Cal-Z	Cal-W	Cal-X
Na_2O	0.62	1.58	0.08	0.53	0.38	0.90	0.55	1.66
MgO	0.52	0.72	0.65	0.44	0.28	0.53	0.95	0.76
Al_2O_3	5.14	4.54	5.39	3.77	3.13	6.42	12.30	20.38
SiO_2	12.02	10.79	14.50	9.55	7.47	14.83	29.48	33.78
P_2O_5	0.09	0.10	0.23	0.04	0.00	0.05	0.13	0.19
K_2O	0.91	1.44	1.12	0.60	0.55	0.98	2.39	1.91
CaO	0.41	1.14	0.43	0.21	0.18	0.36	0.74	3.20
TiO_2	0.19	0.13	0.24	0.14	0.12	0.23	0.57	0.98
MnO	0.02	0.02	0.03	0.03	0.03	0.05	0.03	0.06
Fe_2O_3	30.79	29.38	10.74	28.07	31.19	26.08	13.13	10.55
L.O.I	33.8	30.2	44.9	37.0	36.2	32.1	29.1	15.0
TOT	84.5	80.0	78.3	80.3	79.5	82.5	89.4	88.4
La	5.1	9.5	7.3	4.8	6.2	6.3	27.5	26.9
Ce	8.4	17.2	12.9	8.0	11.0	12.2	54.4	55.9
Pr	0.9	1.8	1.4	0.8	1.2	1.3	5.6	6.3
Nd	3.2	6.6	4.8	2.6	4.2	4.4	19.6	23.9
Sm	0.6	1.1	0.8	0.5	0.8	0.8	3.3	4.8
Eu	0.1	0.3	0.2	0.1	0.2	0.2	0.9	1.0
Gd	0.5	0.8	0.7	0.5	0.5	0.6	2.6	4.3
Tb	0.1	0.1	0.1	0.1	<0.1	<0.1	0.4	0.7
Dy	0.4	0.7	0.5	0.3	0.4	0.5	2.2	3.6
Ho	0.1	0.1	0.1	0.1	<0.1	0.1	0.4	0.7
Er	0.3	0.3	0.4	0.2	0.3	0.4	1.1	1.9
Tm	0.0	0.0	0.0	0.0	<0.05	0.1	0.2	0.3
Yb	0.3	0.3	0.4	0.2	0.3	0.3	1.2	1.9
Lu	0.0	0.0	0.1	0.0	<0.04	0.1	0.2	0.3
∑REE	20.0	38.9	29.6	18.1	25.0	27.2	119.5	132.5
Y/Ho	26.3	22.5	21.4	21.3	0.0	0.0	27.5	22.9
Ce/Ce*	0.9	1.0	0.9	0.9	1.0	0.9	1.0	1.0
Eu/Eu*	1.1	1.3	1.1	1.0	1.1	1.1	1.4	1.1
Gd/Gd*	1.0	1.1	1.2	1.2	0.9	1.1	1.0	1.0
Pr_{SN}/Yb_{SN}	1.1	2.1	1.3	1.3	1.2	1.4	1.5	1.1

Table 5
Major oxides (wt. %) and trace elements (ppm) composition of Fe-oxy-hydroxides from the Paola Ridge.

Sample	Cal-F	Cal-P	Cal-T
Na_2O	0.27	0.07	7.77
MgO	1.11	1.85	1.18
Al_2O_3	9.93	16.51	9.24
SiO_2	20.25	36.12	25.14
P_2O_5	1.96	2.81	0.38
K_2O	1.35	2.50	2.19
CaO	0.48	1.23	0.92
TiO_2	0.38	0.79	0.64
MnO	0.04	0.41	0.08
Fe_2O_3	52.09	24.27	13.51
L.O.I	10.5	7.3	6.5
TOT	98.3	93.9	67.5
La	27.6	48.1	43.8
Ce	77.4	159.6	87.8
Pr	7.9	13.5	9.8
Nd	32.4	53.5	35.5
Sm	6.4	10.5	7.3
Eu	1.3	2.3	1.6
Gd	5.9	9.0	6.4
Tb	0.9	1.5	1.0
Dy	4.6	7.9	5.6
Ho	1.0	1.7	1.1
Er	2.7	4.8	3.3
Tm	0.3	0.7	0.4
Yb	2.1	4.2	2.9
Lu	0.4	0.7	0.5
∑REE	171.0	318.0	207.0
Y/Ho	22.5	22.2	25.6
Ce/Ce*	1.2	1.4	0.9
Eu/Eu*	1.1	1.1	1.1
Gd/Gd*	1.1	1.0	1.0
Pr_{SN}/Yb_{SN}	1.2	1.0	1.1

and 107.6 ppm (Table 2). Highly variable ΣREE contents were detected in the siderite samples as they range from 33.5 to 153.9 ppm (Table 3). Sulfides and Fe-oxy-hydroxides also showed highly variable ΣREE contents ranging from 18.1 to 132.5 ppm and from 170.9 to 318.0 ppm, respectively (Tables 4 and 5). A general enrichment of REE was recognized in the muddy sediments (Table 6) with an average value of 237.7 ppm. The calcite/aragonite concretions were characterized by a slight enrichment of LREE compared to HREE (Pr_{SN}/Yb_{SN} between 0.95 and 1.35). No Ce and Gd anomalies were detected in the calcite/aragonite samples whilst the Eu anomaly was slightly positive (average 1.14). The Y/Ho ratio in the calcite/aragonite (average value of 29.2, Table 2) approaches the chondritic value (≈26; e.g., Pack et al., 2007). The average LREE/HREE ratio (Pr_{SN}/Yb_{SN}) within the siderite concretions is ca. 0.45 and Ce and Gd anomalies are lacking or slightly positive (between 1.00-1.34 and 1.05–1.21, respectively). Siderite samples do not show any Eu anomaly. The siderite samples show near-chondritic Y/Ho ratios as they vary from 25.6 to 38.4 (Table 3). Sulfide concretions display slight enrichments of LREE compared to HREE (average Pr_{SN}/Yb_{SN} = 1.37). Sulfides show a general lack of Ce and Gd as well as Eu anomalies (Table 4). The average Y/Ho value in the sulfide concretions is about 23.6. The Fe-oxy-hydroxide concretions have a rather flat REE pattern (average Pr_{SN}/Yb_{SN} = 1.1). These concretions lack a Gd anomaly while slightly positive Ce and Eu anomalies are present (Table 5). The average Y/Ho ratio of the Fe-oxy-hydroxide concretion is 23.4. Within the muddy sediments the shale-normalized REE pattern typically show weak LREE enrichment compared to HREE (average Pr_{SN}/Yb_{SN} = 1.1–1.2). In particular, mud samples have high HREE depletion compared to LREE (Pr_{SN}/Yb_{SN} up to 1.7). The average Y/Ho ratio for the mud samples is of 25.0 (Table 6).

4.5. Gas and water analyses

Gas samples from fast venting sites (MB14_BC05 and MB14_BC09; Tables 1 and 7; Fig. 1) revealed a chemical composition dominated by CO_2 (up to 98.73% by vol.) and subordinately by N_2 (up to 1.26% by vol.) and methane (<0.06% by vol.). The carbon and oxygen isotopic ratios of CO_2 were −1.8 and −1.1 (V-PDB ‰) and −2.4 and −4.4 (V-PDB ‰), respectively (Table 7).

The chemical composition (in mg L^{-1}) of the water samples collected from the rosettes is reported in Table 8. The Cl^-/Na^+ and Cl^-/Mg^{2+} ratios were all in a narrow range (ca. 1.8 and 15.5, respectively) and similar to that of the present-day seawater (Taylor and McLennan, 1985), whereas the Cl^-/SO_4^{2-} and Cl^-/K^+ ratios were relatively more variable (mean values 5.89 and 46.8, respectively) and lower than that of seawater (ca. 7.2 and 48.6, respectively; CRC, 2005). The concentrations of Br^- and F^- (up to 79 and 2.52 mg L^{-1}, respectively) and the alkalinity (up to 243 mg L^{-1}) were slightly higher than those in the mean ocean water. Free-CO_2 contents were between 11.2 and 14 mmol L^{-1}.

5. Discussion

5.1. Characterization of authigenic minerals

The sub-bottom sediments at Paola Ridge (few cm to few meters below the seafloor, Fig. 2) are characterized by abundant concretions, mainly consisting of calcite/aragonite and siderite (Table 1). Aragonite represents a typical precipitate at methane seeps where

Table 6
Major oxides (wt. %) and trace elements (ppm) composition of muddy sediments from the Paola Ridge.

Sample	Cal-1	Cal-2	Cal-3	Cal-4	Cal-5	Cal-6	Cal-7	Cal-8	Cal-9	Cal-10	Cal-11	Cal-12	Cal-13	Cal-14	Cal-15	Cal-16	Cal-17	Cal-18	Cal-19	Cal-20	Cal-21	Cal-22	Cal-23	Cal-24	Cal-25	Cal-26	Cal-27	Cal-28	Cal-29	Cal-30	Cal-31	Cal-32
Na_2O	0.2	9.0	0.0	0.2	4.3	8.5	3.0	0.0	0.3	0.0	6.7	0.0	0.0	1.2	6.9	0.0	12.2	0.0	6.8	4.5	8.3	0.0	11.6	7.2	8.6	7.4	0.2	0.6	0.3	0.2	0.0	0.2
MgO	2.0	0.4	1.9	0.9	1.4	0.6	1.1	1.4	2.1	2.3	1.2	1.1	2.3	0.3	1.9	2.3	0.7	1.1	1.2	0.8	0.5	1.8	0.9	1.3	0.9	1.1	2.9	1.2	2.6	2.5	1.5	2.6
Al_2O_3	20.8	6.2	19.8	23.1	16.1	8.2	11.8	15.3	15.2	17.7	13.5	20.6	20.1	10.3	10.7	18.1	3.0	21.3	14.2	15.6	10.1	20.3	3.6	12.8	10.2	12.7	13.7	19.7	14.0	14.0	19.2	16.1
SiO_2	52.5	16.8	51.3	54.5	39.9	21.5	28.5	38.7	41.0	46.8	34.4	53.3	52.5	31.6	27.6	44.9	7.7	53.9	35.0	35.8	24.1	53.4	9.1	32.8	27.3	32.8	35.1	54.7	38.2	36.1	51.9	41.3
P_2O_5	0.2	0.1	0.2	0.2	0.1	0.1	0.2	0.2	0.2	0.2	0.1	0.2	0.2	0.1	0.1	0.4	0.1	0.2	0.2	0.1	0.1	0.3	0.1	0.1	0.1	0.1	0.1	0.3	0.2	0.1	0.3	0.1
K_2O	3.7	1.8	3.7	4.1	3.2	2.3	2.0	2.9	3.3	3.3	2.9	3.1	3.8	3.4	2.5	3.5	0.9	3.3	2.9	2.8	2.2	3.7	1.1	2.8	2.5	2.7	2.7	5.9	2.8	2.9	3.5	3.1
CaO	1.5	0.9	1.1	1.9	1.2	0.7	1.6	1.2	7.7	8.8	1.2	0.9	2.8	0.8	5.3	5.6	14.1	1.1	1.1	1.2	0.7	1.4	18.2	1.3	1.0	1.0	19.9	1.9	19.0	18.9	1.4	13.1
TiO_2	1.2	0.8	1.2	1.3	1.1	0.9	0.5	0.9	0.9	1.0	1.0	1.0	1.2	0.3	0.8	1.0	0.3	1.1	1.0	1.1	0.7	1.1	0.4	0.9	0.9	0.9	0.8	0.9	0.8	0.8	1.1	0.9
MnO	0.1	0.1	0.0	0.0	0.0	0.1	0.5	0.0	0.1	0.1	0.1	0.0	0.1	0.1	0.1	0.1	0.0	0.0	0.0	0.0	0.1	0.1	0.0	0.0	0.1	0.0	0.1	0.1	0.1	0.1	0.1	0.1
Fe_2O_3	7.1	6.0	7.3	3.6	5.9	5.6	24.4	6.1	8.0	7.0	6.4	4.9	7.3	12.7	6.1	11.7	2.4	3.6	5.8	3.3	6.9	7.0	3.2	6.4	6.3	6.7	6.0	5.7	6.6	5.9	10.0	7.1
L.O.I	6.6	5.8	6.8	6.6	6.4	6.4	17.2	8.4	10.8	10.0	6.7	9.6	7.2	19.9	11.2	9.6	24.2	10.7	6.2	9.1	16.0	8.0	10.0	9.3	6.2	6.9	17.0	6.1	12.8	16.1	8.4	13.2
TOT	95.8	47.8	93.2	96.4	79.8	54.7	90.7	75.2	89.6	97.3	74.3	94.6	97.4	80.6	73.1	97.0	65.5	96.4	74.4	74.4	69.6	97.1	58.3	74.9	64.1	72.4	98.4	97.1	97.5	97.6	97.4	97.8
La	50.8	54.4	54.1	53.2	52.1	60.4	29.6	51.0	41.7	47.8	54.2	53.9	51.1	116.7	44.5	48.7	29.7	60.4	44.7	51.9	49.6	52.3	51.3	45.4	47.4	51.7	39.7	65.8	35.2	35.4	42.4	36.9
Ce	101.6	105.8	105.7	96.9	101.4	118.7	58.8	100.7	83.1	87.9	104.9	112.3	98.0	204.9	83.3	91.9	56.0	117.9	100.7	111.5	98.3	115.5	111.6	93.2	98.8	112.4	77.1	130.0	68.6	68.3	86.6	75.3
Pr	10.9	11.5	11.1	9.7	10.7	12.8	6.5	10.9	8.9	9.6	11.2	11.7	10.9	21.5	9.6	9.9	6.1	12.5	10.2	10.8	9.5	11.2	10.9	10.0	10.6	11.0	8.5	13.7	7.5	7.7	9.4	8.3
Nd	41.5	38.7	42.5	35.2	39.6	45.7	24.6	41.2	34.1	36.4	43.2	38.2	41.6	74.9	33.7	34.4	23.8	41.9	34.6	39.9	33.3	38.7	38.9	33.6	36.8	39.3	31.7	47.2	28.7	28.2	35.1	31.1
Sm	7.3	7.6	7.4	6.2	7.5	8.7	4.9	7.2	5.9	6.5	7.4	7.5	7.5	11.8	6.6	6.2	4.2	7.6	6.9	7.0	6.5	7.9	7.3	7.1	7.2	7.6	5.9	9.1	5.2	5.5	6.9	6.0
Eu	1.5	1.7	1.5	1.4	1.5	1.8	1.1	1.5	1.2	1.3	1.5	1.3	1.5	1.0	1.3	1.3	0.9	1.3	1.4	1.4	1.2	1.6	1.5	1.4	1.5	1.5	1.2	1.8	1.3	1.1	1.5	1.3
Gd	6.2	6.5	6.5	4.8	6.4	7.8	5.1	6.0	5.3	5.7	6.6	5.6	6.2	9.2	5.7	5.6	4.0	5.9	5.6	5.6	4.9	6.6	6.4	6.3	6.4	6.5	5.2	7.6	4.6	4.7	5.6	5.1
Tb	1.0	1.0	1.0	0.8	1.0	1.3	0.8	0.9	0.8	0.9	1.0	0.9	1.0	1.4	0.8	0.8	0.6	0.9	0.9	0.8	0.8	1.1	1.0	0.9	1.0	1.1	0.8	1.1	0.8	0.8	0.9	0.8
Dy	4.9	5.7	5.7	4.0	5.4	6.6	5.0	4.4	4.5	4.5	5.1	4.4	5.1	7.5	4.3	4.9	3.3	5.0	4.6	5.1	4.6	5.5	5.6	5.1	5.6	6.3	4.5	6.0	4.0	4.1	5.2	4.4
Ho	1.1	1.2	1.2	0.9	1.1	1.4	1.0	1.0	1.0	0.9	1.1	0.8	1.0	1.5	1.0	1.0	0.7	1.0	1.0	0.9	0.9	1.3	1.1	1.1	1.2	1.3	0.9	1.1	0.8	0.8	1.0	0.8
Er	3.3	3.4	3.5	2.6	3.4	4.1	3.0	2.8	2.6	2.8	3.1	2.3	3.1	4.3	2.6	2.7	2.0	2.7	2.8	2.7	2.3	3.3	3.1	2.7	2.9	3.3	2.6	3.2	2.2	2.3	2.8	2.4
Tm	0.4	0.5	0.5	0.3	0.4	0.6	0.4	0.4	0.4	0.4	0.4	0.4	0.4	0.6	0.4	0.4	0.3	0.4	0.4	0.4	0.4	0.5	0.5	0.4	0.5	0.5	0.4	0.5	0.3	0.3	0.4	0.4
Yb	2.8	3.1	3.4	2.5	2.9	3.5	2.6	2.5	2.4	2.5	3.1	2.6	2.9	4.0	2.6	2.2	1.7	2.4	2.6	2.5	2.7	3.3	2.7	2.5	3.2	2.9	2.5	3.3	2.4	2.3	2.8	2.4
Lu	0.4	0.4	0.5	0.4	0.4	0.6	0.4	0.4	0.4	0.4	0.4	0.4	0.5	0.6	0.4	0.4	0.3	0.4	0.4	0.4	0.4	0.5	0.5	0.4	0.5	0.6	0.4	0.4	0.3	0.3	0.4	0.3
∑REE	233.8	241.5	244.5	218.7	234.0	273.8	143.7	231.0	192.1	207.4	243.2	242.1	230.8	459.8	196.9	210.4	133.4	260.2	216.7	240.9	215.2	249.3	242.3	210.0	223.5	245.8	181.4	290.9	161.9	161.9	201.1	175.5
Y/Ho	23.8	23.8	24.9	21.8	22.8	25.7	28.2	23.2	23.6	27.1	25.6	22.3	26.3	26.3	23.8	23.7	24.9	21.8	25.5	24.2	23.1	22.3	24.1	23.5	24.4	23.7	27.8	30.0	27.5	30.0	26.0	28.8
Ce/Ce*	1.0	0.9	1.1	1.1	1.0	1.0	1.0	1.0	1.0	1.0	1.1	0.9	1.0	1.0	0.9	0.9	1.0	0.9	1.0	1.1	1.0	1.0	1.1	0.9	0.9	1.1	1.0	0.9	1.0	0.9	1.0	1.0
Eu/Eu*	1.1	1.1	1.1	1.2	1.1	1.0	1.0	1.1	1.1	1.0	1.0	0.9	1.1	0.4	1.0	1.1	1.1	0.9	1.1	1.1	1.0	1.0	1.1	1.1	1.0	1.0	1.1	1.1	1.2	1.0	1.1	1.1
Gd/Gd*	1.0	1.1	1.0	1.0	1.1	1.0	1.1	1.1	1.1	1.1	1.1	1.0	1.0	1.0	1.1	1.1	1.1	1.0	1.0	1.1	1.0	1.0	1.0	1.1	1.0	1.0	1.1	1.1	1.0	1.0	1.0	1.0
Pr_{SN}/Yb_{SN}	1.2	1.2	1.0	1.2	1.2	1.2	0.8	1.4	1.2	1.2	1.1	1.4	1.2	1.7	1.2	1.4	1.2	1.7	1.3	1.4	1.1	1.1	1.3	1.3	1.1	1.2	1.1	1.3	1.0	1.1	1.1	1.1

Table 7
Chemical composition (in % by vol.) and $\delta^{13}C$-CO_2 and $\delta^{18}O$-CO_2 V-PDB values of the venting gases.

Sampling station	CO_2 (%)	N_2 (%)	O_2 (%)	Ar (%)	CH4 (%)	$\delta^{13}C^2_{CO}$ (‰)	$\delta^{18}O^2_{CO}$ (‰)
MB14 BC05	98.73	1.08	0.11	0.026	0.056	−1.1	−4.4
MB14 BC09	98.61	1.26	0.053	0.031	0.051	−1.8	−2.4

Table 8
Chemical composition of the seawater recovered by rosette samplers. Total alkalinity and ion contents are in mg L^{-1} while free-CO_2 is in mmol L^{-1}.

	Alk.	F^-	Cl^-	Br^-	NO_3^-	SO_4^{2-}	Ca^{2+}	Mg^{2+}	Na^+	K^+	NH_4^+	CO_2
MB14_ROS05	232	1.95	23606	61	11.5	3876	482	1512	12837	598	24.28	11.8
MB14_ROS06	232	1.20	23413	79	n.d.	3901	507	1527	12874	512	n.d.	11.2
MB14_ROS07	231	2.32	23639	72	n.d.	3920	506	1494	12692	483	n.d.	14.0
MB14_ROS08	159	2.52	23323	74	9.0	3918	521	1482	12575	473	n.d.	12.9
MB14_ROS09	243	n.d.	23132	70	20.1	3824	486	1499	12896	544	n.d.	11.9

Alk.: total alkalinity.
n.d.: not determined.

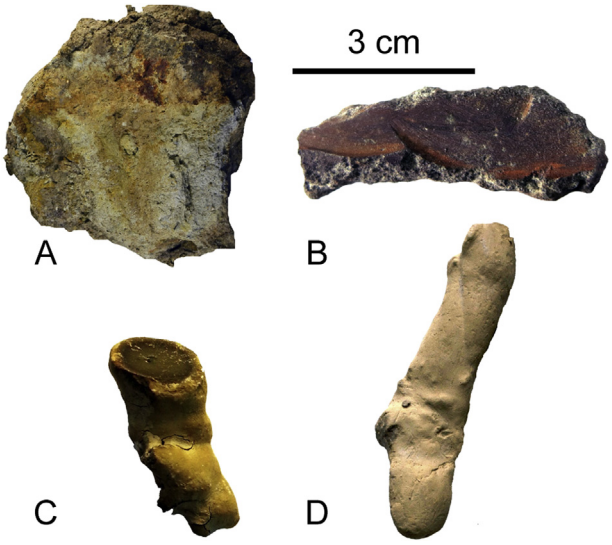

Fig. 3. Carbonate concretions: **A)** Aragonite/calcite concretion (Sample Cal-N). **B**) Siderite crust (Sample Cal-E). **C**) Section of a siderite tubular concretion (Sample Cal-MB4). **D**) Siderite tubular concretion (Sample Cal-G) showing the typical whitish outer crust.

microbial activity induces the increase of alkalinity in pore solutions by AOM and the consequent precipitation of authigenic carbonates (e.g., Taviani, 2001; Peckmann and Thiel, 2004; Campbell et al., 2008; Taviani et al., 2015). At methane seeps, aragonite precipitation is thought to be favored by the presence of sulfate ions, which on the other hand inhibit dolomite precipitation (e.g., Magalhães et al., 2012; Zhang et al., 2012). Therefore, aragonite concretions can be related to a genetic environment close to the seafloor characterized by high alkalinity and sulfate concentration (e.g., Peckmann et al., 2009; Hu et al., 2014). The precipitation of authigenic aragonite and calcite at Paola Ridge only occurs within the sediments of D1 and D2 diapirs, near the seafloor within the SMTZ (Rovere et al., 2014, 2015) during periods of moderate to intense seepage when SMTZ migrates upward. In the calcite/aragonite samples, dolomite is only found as thin crust lining the calcite/aragonite concretions and it is likely precipitated at a different stage of the seepage. Precipitation of dolomite is indeed favored by low concentrations of sulfate (Magalhães et al., 2012) and therefore, it is unlikely to form together with aragonite or at present day conditions with up to 3918 mg L^{-1} of SO_4^{2-} in the bottom seawater (Table 8). Nevertheless, recent studies demonstrated how high sulfide concentration, rather than low sulfate, favors dolomite precipitation at sites of methane seepage (Zhang et al., 2012; Taviani et al., 2015). At times of intense seepage the SMTZ is pulled further upward through the subseafloor sediment and the sulfates in the shallow sediments are more efficiently consumed releasing Mg-ions. Consequently, under such conditions the Mg/Ca ratio increases and dolomite precipitates (e.g., Magalhães et al., 2012). In this scenario the precipitation of dolomite likely records an additional surge in seepage activity following the first seepage increase responsible for aragonite/calcite concretion precipitation.

Pyrite is another common authigenic mineral found at methane seeps (e.g., Peckmann and Thiel, 2004; Cavalazzi et al., 2014) where the bacterial-mediated sulfate reduction fosters the precipitation of pyrite rather than that of siderite (e.g., Curtis et al., 1972). Interestingly, in the study area, pyrite and siderite are characteristic of the core sediments from the RMV and R1MV structures, where carbonate/aragonite concretions are lacking (Fig. 2). However, pyrite and siderite never co-occur in the same concretion (Table 1; Figs. 2–6). Mozley and Wersin (1992) demonstrated that siderite precipitation is favored by suboxic conditions coupled with low organic matter content and low sedimentation rate, and strongly reducing conditions. Generally, siderite formation is favored by low sulfide activity under anoxic conditions (Taylor and Curtis, 1995; Rovere et al., 2015) and therefore occurs outside the sulfate reduction zone, where organic matter fermentation (i.e. methanogenic zone) occurs (Matsumoto, 1989; Carothers et al., 1988; Hicks et al., 1996; Hein et al., 2006; Wittkop et al., 2014). The methanogenic zone provides conditions suitable for preferential precipitation of siderite (e.g., Berner, 1981; Mozley and Wersin, 1992) with respect to that of pyrite (e.g., Rovere et al., 2015). Therefore, the co-occurrence of pyrite and siderite in the same sampling sites has to be explained with the dynamics of the environment itself and must be related to fluctuation in the intensity of fluid seepage and gas venting. On RMV and R1MV structures, during periods of sustained gas venting, the abundance of sulfate within the sea water increases (Table 8) and sulfate reduction favors pyrite precipitation and would inhibit siderite precipitation. This hypothesis is supported by the concentrations of SO_4^{2-} at the bottom seawater (Table 8), which were >20% higher than that of the Mediterranean Sea. During periods of lower gas discharges the SMTZ deepens and decreased sulfide concentration is associated with the increase of dissolved Fe^{2+} in the shallow sub-bottom sediments, thus facilitating the precipitation of siderite (e.g., Curtis et al., 1972).

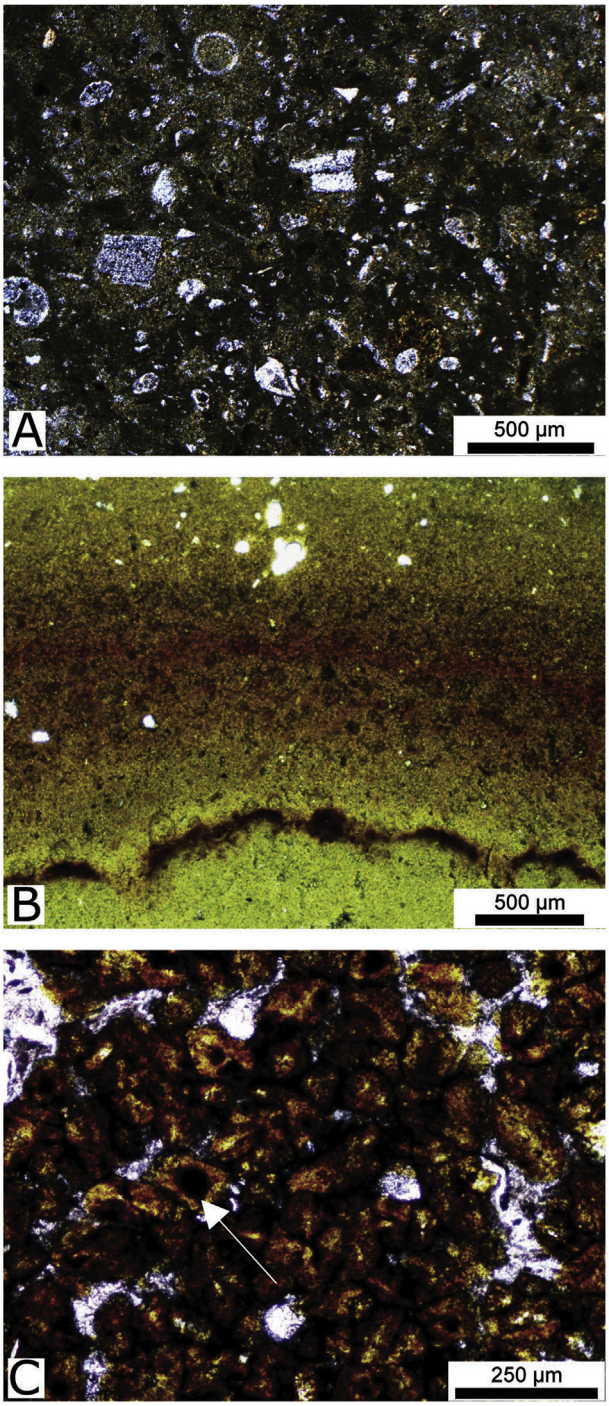

Fig. 4. Transmitted light photomicrographs of the carbonate concretions. **A**) Calcite/aragonite concretion with foraminifera remains and abundant terrigenous material. **B**) Transversal section of sample Cal-G showing concentric layering of the concretion; outer part is toward the top of the figure. The bulk of the concretion is micro-to meso-sparitic siderite. **C**) Interlocking crystals of siderite with a turbid core (white arrow) in sample Cal-FF. A: cross-polarized light; B–C: plane-polarized light.

5.2. Isotopic composition of carbonates and origin of mineralizing fluids

The calcite/aragonite concretions are characterized by negative $\delta^{13}C$ values (−48.8‰ to −26.3‰ V-PDB; Table 1) indicating ^{13}C-poor dissolved inorganic carbon (DIC) issued from methane oxidation as the source of carbon (e.g., Whiticar, 1999; Peckmann and Thiel, 2004). The variable carbon isotopic composition of the samples is likely indicative of mixing between thermogenic and biogenic methane-rich fluids (e.g., Mazzini et al., 2005; Peckmann and Thiel, 2004), or fractionation processes as the methane-rich fluids migrate.

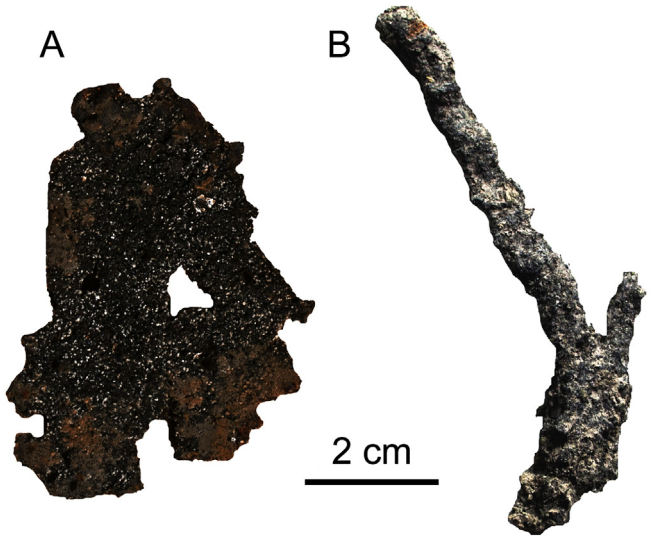

Fig. 5. Sulfide crusts in the Cal-O sample (**A**) and sulfide tubular concretions in sample Cal-Q (**B**).

Siderite concretions, on the other hand, show highly positive $\delta^{13}C$ values (between 3.2‰ and 10.6‰ V-PDB), which suggests precipitation from fluids with ^{13}C-rich DIC. These positive $\delta^{13}C$ values can be diagnostic of precipitation in the methanogenic zone (e.g., Curtis and Coleman, 1986; Mozley and Wersin, 1992; Whiticar, 1999). Whilst the $\delta^{18}O$ values of calcite/aragonite concretions ranged between 1.4‰ and 5.5‰ V-PDB, the average $\delta^{18}O$ for siderite is greater than 9‰ V-PDB. At the average value of the present-day bottom water temperature (13.8 °C) and $\delta^{18}O$ value of water (1.5‰) in the Mediterranean Sea, the theoretical $\delta^{18}O$ values of calcite (Kim and O'Neil, 1997), aragonite (Kim et al., 2007), dolomite (Vasconcelos et al., 2005) and siderite (Fernandez et al., 2016) precipitated in isotopic equilibrium with seawater are expected to be of 1.5‰, 2.2‰, 4.5‰ and 5.6‰ (V-PDB), respectively. The $\delta^{18}O$ values obtained from the Paola Ridge carbonates approach the theoretical values except for those of siderite, which are mostly enriched in ^{18}O by 3–4‰.

Whilst general ^{13}C enrichment can be explained with the incorporation of heavy C derived from methanogenesis the enrichment of ^{18}O is more complicated. The ^{18}O enrichment in carbonates has previously been explained by different processes occurring in the sedimentary environment, as follows: 1) dissociation of gas hydrates that releases ^{18}O-rich water in the sediments (e.g., Matsumoto, 1989; Bohrmann et al., 1998; Aloisi et al., 2000; Maekawa, 2004; Hein et al., 2006); 2) interaction with hydrothermal fluids that may yield values as high as 6.5‰ (Clayton and Epstein, 1961); 3) dehydration of clay minerals at great burial depths (Dählmann and de Lange, 2003); 4) crustal/igneous CO_2 circulation (Muehlenbachs and Hodges, 1978; Clayton and Epstein, 1961; Cocker et al., 1982); 5) precipitation of carbonates during glacial times when lower temperatures and isotopically heavier seawater caused a 3–4‰ $\delta^{18}O$-shift of carbonates in the Mediterranean Sea (e.g., Vergnaud-Grazzini, 1971). Other sources of heavy oxygen can be due to the circulation of deep crustal water (e.g., Lécuyer and Allemand, 1999). Lécuyer and Allemand (1999) discussed how the significant enrichment in ^{18}O of ophiolitic

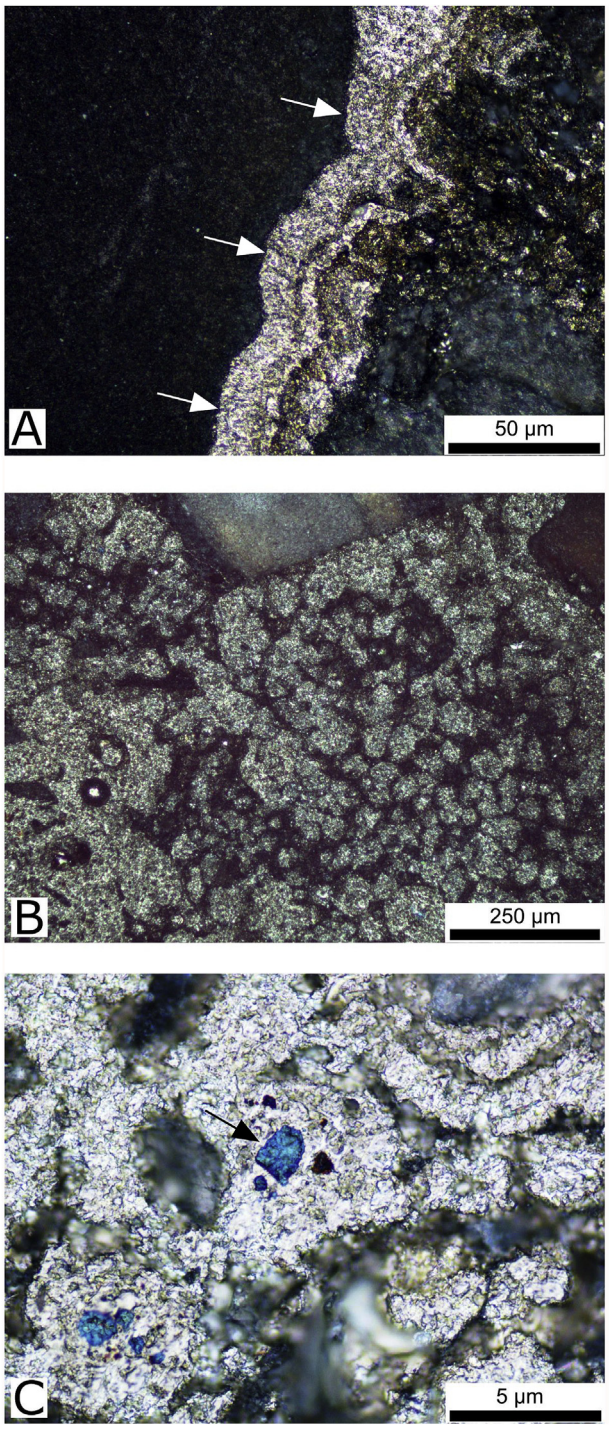

Fig. 6. Reflected light photomicrographs of the sulfide concretions (Sample Cal-S). **A**) Crustiform sulfides pyrite/marcasite (arrows). The dark area on the left of the figure is primary porosity. **B-C**) Aggregate of anhedral and granular sulfides (pyrite/marcasite); arrows point to a grain of covellite/chalcocite.

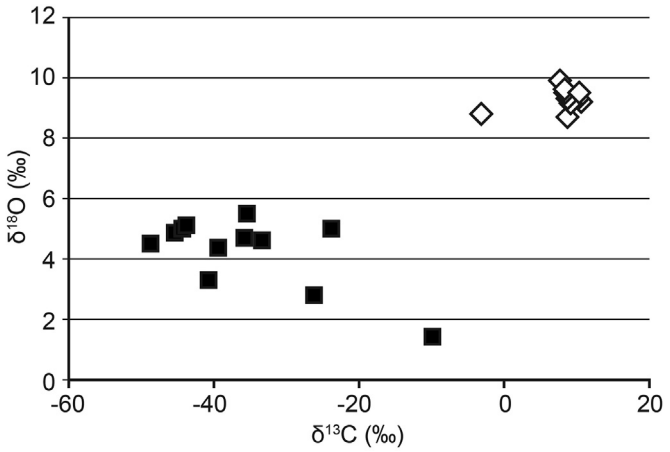

Fig. 7. Siderite (diamonds) and calcite/aragonite (squares) concretions isotopic composition ($\delta^{13}C$ and $\delta^{18}O$).

complexes (up to 8‰; Lécuyer and Fourcade, 1991) would explain the shift toward higher $\delta^{18}O$ values of the circulating water. These authors proved that at depth between 1.5 and 3.5 km the increase of temperature induces a large oxygen fractionation between the igneous rocks and seawater resulting in lower $\delta^{18}O$ values within the rocks at the expense of the reacting water.

The presence of active venting of CO_2 along RMV and R1MV (Tables 1 and 7) suggests that the likely source of heavy oxygen isotopes in siderite concretions can be related to deep fluids circulation (e.g., Clayton and Epstein, 1961; Lécuyer and Allemand, 1999; Lietard and Pierre, 2009). The presence of CO_2-rich gas discharges, characterized by $\delta^{13}C$-CO_2 values slightly lower than −1‰ V-PDB (Table 7), certainly suggests the presence of a deep-seated source feeding these gas vents. Such values are indeed similar to those found in the fumarolic gas discharges from the Island of Volcano (e.g., Paonita et al., 2002) and Solfatara, Somma-Vesuvius and related submarine emissions (e.g., Chiodini et al., 2001; Caliro et al., 2007; Vaselli et al., 2011; Passaro et al., 2016) and many gas vents distributed along the peri-Tyrrhenian strip (e.g., Minissale et al., 1997) of the Italian peninsula. The origin of the peri-Tyrrhenian vents is mainly related to thermometamorphic processes of marine limestone, although small contributions from a magmatic source cannot be excluded. In addition, the concentrations of free-CO_2 within the Paola Ridge bottom sea water showed relatively high values, which corroborate the contribution of deep-seated CO_2 to the gas discharges. At Paola Ridge CO_2-rich-gas venting was only recorded along the RMV and R1MV structures suggesting a possible interaction between CO_2 venting and siderite precipitation and therefore a likely ^{18}O enrichment of the iron carbonates related to crustal/igneous CO_2 circulation (Muehlenbachs and Hodges, 1978; Clayton and Epstein, 1961; Cocker et al., 1982). Although CO_2-rich sediments are usually considered unsuitable for carbonate precipitation, siderite precipitation has previously been reported at the oxic-suboxic transition in places where venting CO_2 reacts with reduced iron within the sediments (Bahrig, 1988; Mozley and Wersin, 1992).

The Y/Ho ratio is considered a strong indicator of deep fluid circulation and REE fractionation (e.g. Klinkhammer et al., 1994; Bau and Dulski, 1999). Y and Ho are considered chemical twin and therefore are expected to have a similar geochemical behavior in seawater (e.g., Zhang et al., 1994; Bau, 1996; Nozaki et al., 1997). The geochemical twins Y and Ho remain tightly coupled in common igneous rocks and epiclastic sediments, leading to the maintenance of the chondritic Y/Ho ratio of about 26–28 (Bau, 1996 and references therein). On the contrary, modern seawater and related marine precipitates are often characterized by super-chondritic (up to 90) Y/Ho ratio (Bau, 1996; Zhang et al., 1994; Bau et al., 1997; Nozaki et al., 1997). The carbonates from Paola Ridge show average Y/Ho ratio of ca. 31 (Tables 3 and 4), close to chondritic values and lack the linear correlation between Y/Ho and La anomaly characteristic of modern seawater signatures (e.g., Bau, 1996; Webb and Kamber, 2000; Allwood et al., 2010; Franchi et al., 2015). Deep

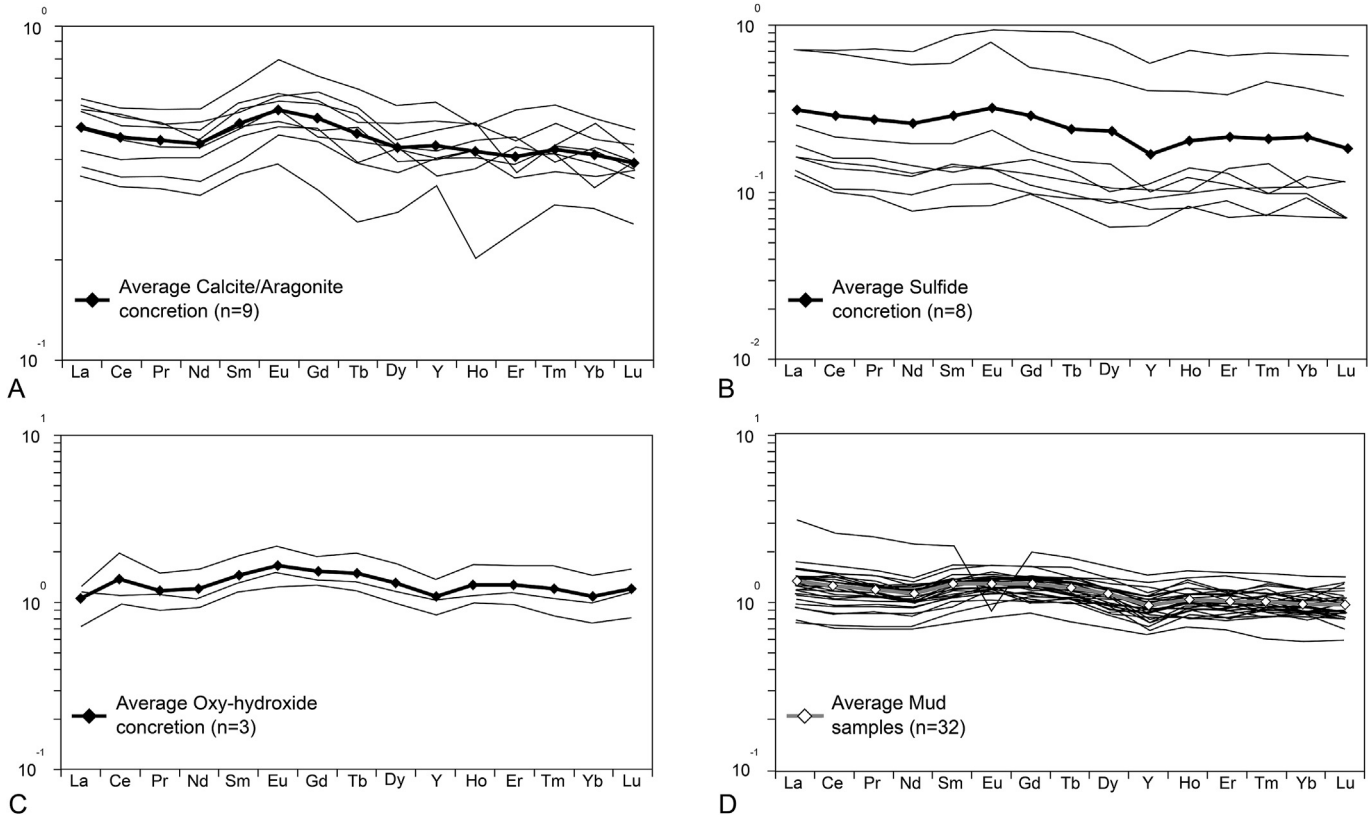

Fig. 8. PAAS-normalized REE patterns of calcite/aragonite (A), sulfides (B), Fe-oxy-hydroxides (C) and muddy sediments (D).

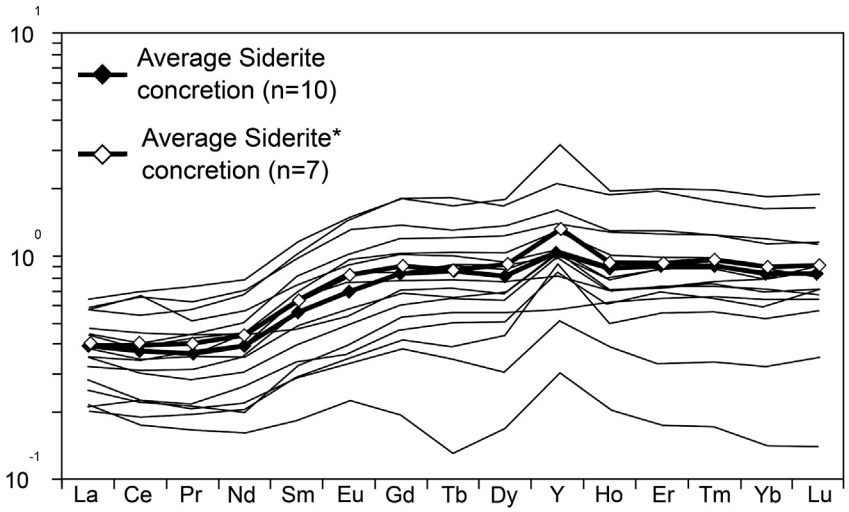

Fig. 9. PAAS-normalized REE patterns of siderite concretions (* refers to the second series of analyses, see Table 3).

fluids, including hydrothermal fluids, have higher concentrations of REE compared to seawater and chondritic Y/Ho ratios (e.g.,Klinkhammer et al., 1994; Bau and Dulski, 1999). Venting of deep-seated fluids may therefore induce a Y/Ho near-chondritic ratio coupled with ΣREE enrichment and sensible increase of LREE contents (e.g., Michard, 1989; Klinkhammer et al., 1994; Bau and Dulski, 1999).

Rovere et al. (2014) performed AMS radiocarbon age dating on chemosymbiotic bivalves collected from the very shallow sediments of the Paola Ridge (alongside diapirs D1 and D2, down to about 1 m below the seafloor) revealing calibrated age ranging between 440 BP and 13,710 BP suggesting a prolonged seepage activity. Notwithstanding, investigations on present day venting gas and bottom seawater highlighted the absence of substantial concentrations of methane (Tables 7 and 8). Normally, at sites of vigorous methane seepage the presence of methane can be detected within samples of water throughout the water column up to very shallow depth (see Sommer et al., 2015) and gas bubbles at the surface might still contain up to 25% of the original methane (Sommer et al., 2015; Schneider von Deimling et al., 2015).

Nevertheless, as far as the sampled waters are concerned, their chemical composition is approaching that of the oceanic water reported by Taylor and McLennan (1985), though slightly more alkaline (Table 8), as typical of relatively closed basin such as the Mediterranean Sea. The general lack of methane in both venting gases and bottom sea water at Paola Ridge suggests that the methane seepage, active for the last 10 k year (40 k years according to Rovere et al., 2015), is currently minimal.

5.3. Redox conditions during sedimentation

The distribution of the different authigenic mineral concretions is likely reflecting a biogeochemical zonation of the sediments from oxic conditions to AOM/sulfate reduction to methanogenesis (Rovere et al., 2015). The fluctuation of seepage activity and change in fluid composition likely influenced the redox conditions during the precipitation of the authigenic minerals.

The REE pattern of marine carbonates can be used as a geochemical proxy for the reconstruction of fluid composition and physical-chemical variations (Elderfield and Greaves, 1982; German and Elderfield, 1990; Bau et al., 1997; Franchi et al., 2015, 2016 and references therein). Several studies showed that REE are not affected by fractionation processes during precipitation of aragonite and calcite (see discussion in Rongemaille et al., 2011) whereas REE distribution tends to vary significantly in sediments according to the redox variations within the pore water (e.g., Haley et al., 2004). Nevertheless, the use of carbonates as a proxy for the REE content of ancient seawater is complicated by possible modification due to the presence of: i) REE-bearing terrigenous components (Goldstein and Jacobsen, 1988; Elderfield et al., 1990); ii) Fe-Mn-oxy-hydroxides (Bau et al., 1996; Bayon et al., 2004) and iii) phosphates, which might have a non-uniform REE incorporation (German and Elderfield, 1990; Byrne et al., 1996). To avoid the terrigenous contamination, Rongemaille et al. (2011) proposed the usage of weak acetic acid solution (5% v/v) for quantitative leaching of carbonate samples. Nevertheless, the authors concluded that a weak acid leaching is not appropriate to achieve complete dissolution of siderite. An alternative method suggests the stepwise dissolution of carbonates by means of 5% v/v acetic acid with removal of the initial and final leachates (Zhang et al., 2015). Also in this case the authors do not mention the efficiency of the method in leaching siderite. Hence, a total dissolution method has been adopted in this work and possible contaminations were verified by using a correlative method (Fig. 10).

Normalized REE patterns of the calcite/aragonite concretion under investigation (Fig. 8A) displayed a non-marine seawater trend (e.g., Zhang and Nozaki, 1996). This particular pattern can be due to the presence within carbonate of terrigenous matter, in particular clay minerals, which are able to mask the seawater signature (e.g., Murray et al., 1991; Oliver and Boyet, 2006). Al_2O_3, SiO_2, Zr and Rb distributions are considered proxies for concentrations of terrigenous matter since they closely correlate with the clay content. Despite the high Al_2O_3 and SiO_2 contents (weight % on the bulk sample; Table 2), there is no clear correlation ($R^2 = 0.52$ and 0.54, respectively) with LREE and ΣREE (Fig. 10A–D). On the other hand, Zr and Rb are weakly correlated with ΣREE (Fig. 10F and G), suggesting a possible contribution from acid-leached terrigenous minerals (see Zhang et al., 2015) to the overall REE budget (Fig. 10A–G). Other potential contaminants, such as Fe- and P-compounds (German and Elderfield, 1990; Bau et al., 1996; Reynard et al., 1999; Bayon et al., 2004; Bau and Koschinsky, 2009) do not show significant correlations with ΣREE and LREE (Fig. 10H–I) in the calcite/aragonite concretions. Apart from potential contamination of siliciclastic matter, a flat REE pattern coupled with the lack of a Ce anomaly might indicate that the calcite/aragonite concretions precipitated within relatively highly alkaline pore water (e.g., Pourret et al., 2008) and incorporated high amounts of organic matter brought into solution during the leaching procedure (Zhang et al., 2015). The leaching of adsorbates such as organic matter might induce a weakening of the Ce anomaly and decrease the overall Y/Ho ratio (Zhang et al., 2015). The hypothetical mixing patterns between the limestone and Fe-oxy-hydroxide components do not produce any sensible variation in the REE fractionation, even though the REE content considerably increases (Fig. 11A). Both limestone and Fe-oxy-hydroxide REE patterns are relatively flat (average $Pr_{SN}/Yb_{SN} = 1.10$ and 1.01, respectively) with a slight MREE enrichment ($Gd_{SN}/Yb_{SN} = 1.28$ and 1.45, respectively), which is typical of precipitates formed in oxic to sub-oxic pore water (Haley et al., 2004). Under such conditions the REE pattern lacks Ce and Gd anomalies and the precipitates are expected to inherit these characteristics from the reacting water.

The REE patterns of the siderite concretions (Fig. 9) show a general depletion of LREE and a quasi-marine trend (cf. Zhang and Nozaki, 1996) with strong HREE enrichment. Within siderite samples Al_2O_3, SiO_2, Rb and Zr do not correlate with LREE and ΣREE (Fig. 10A–E) ruling out any terrigenous contamination. Similarly, contamination by Fe-Mn-oxy-hydroxides and phosphates can be considered negligible or absent as no correlation between Fe and P and LREE and ΣREE is recorded (Fig. 10H and I). The strong LREE fractionation found in the siderite concretions points toward a slow formation close to the exchange equilibrium of adsorbed/dissolved REE and Y (Bau and Dulski, 1996) under reducing conditions (see Fig. 1 in Mozley and Wersin, 1992). The prolonged anoxic conditions, high pore water alkalinity and high Fe concentration are also suggested by the enrichment of MREE (Haley et al., 2004) and the lack of a Ce anomaly (see discussion below). The siderite precipitation rate is eight orders of magnitude slower than that of calcite (Jimenez-Lopez and Romanek, 2004) and therefore, the formation of siderite concretions is likely to be stable under supersaturated conditions fostering LREE fractionation. The hypothetical siderite and Fe-oxy-hydroxide mixing (Fig. 11B) shows that i) the increase of Fe-oxy-hydroxides incorporation in the siderite concretions might induce a general increase of LREE concentration and a flattening of the REE pattern similar to that detected in the average limestone concretions and ii) siderite and Fe-oxy-hydroxide have an opposite rate of Y complexation and similar HREE concentration. The lack of LREE fractionation in the Fe-oxy-hydroxides from Paola Ridge (Fig. 8) may be due to a rapid deposition (e.g., Bau and Dulski, 1996) under oxic conditions.

The Ce anomaly is a valuable tool for unraveling the redox condition at time of authigenic mineral precipitation (e.g., Hu et al., 2014). The value of the Ce anomaly is thought to be indicative of redox state (Haley et al., 2004 and citations therein), being negative (ca. 0.2–0.4) under oxygenated conditions and positive under anoxic conditions (e.g., Olivier and Boyet, 2006; Hu et al., 2014; Tostevin et al., 2016). Nevertheless, it has been observed that the presence/absence of a negative Ce anomaly in authigenic methane-imprinted carbonates can be due to mineral formation in high pore water alkalinity where organic matter occurs (Pourret et al., 2008; Kim et al., 2012) to the intermittent oxygenation of sediments (Birgel et al., 2011; Hu et al., 2014) and can be also affected by leaching procedure (Zhang et al., 2015). Discontinuous fluids discharge and downward flow of sea water during periods of reduced seepage can produce carbonates with a particular geochemical signature and disguise the original Ce anomaly (Solomon et al., 2008; Kim et al., 2012; Hu et al., 2014) resulting in a Ce/Ce* ratio close to 1. The lack of a Ce anomaly, typical of both limestone and siderite at the Paola Ridge (Tables 2 and 3) can be thus explained by discontinuity of methane seepage and sustained conditions of high alkalinity and high organic matter content.

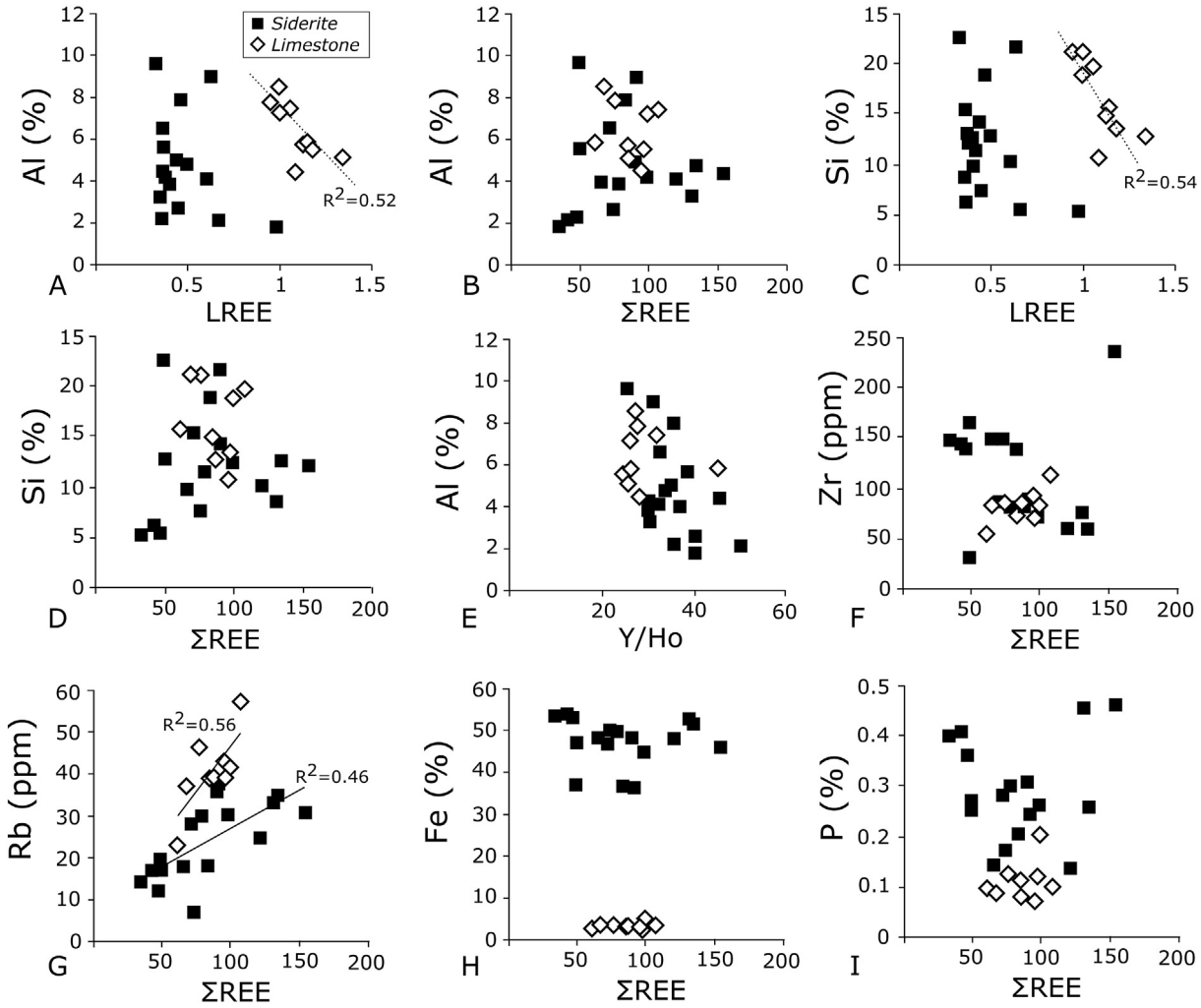

Fig. 10. Binary diagrams of terrigenous contaminant proxies versus ΣREE, LREE (Pr/Yb) and Y/Ho for the calcite/aragonite and siderite concretions.

Moreover, in presence of high organic matter contents, the high alkalinity of the pore water and the preferential uptake of dissolved Ce(IV) by organic compounds induces a Ce enrichment in the authigenic fraction (Pourret et al., 2008; Kim et al., 2012; Hu et al., 2014). As discussed above, siderite concretions at Paola Ridge show evidences of precipitation within the fermentation zone (e.g., Irwin et al., 1977; Matsumoto, 1989; Wittkop et al., 2014). Authigenic siderite formed within the methanogenesis zone, where metabolic activity of microbial consortia triggers the precipitation of authigenic carbonates (e.g., Chafetz and Buczynski, 1992; Monty, 1995), may thus lack a consistent Ce anomaly as shown by Paola Ridge samples.

The variation in redox condition during the formation of authigenic carbonates can be outlined by using specific trace elements such as Mo and U (e.g., Hu et al., 2014). In well-oxygenated water Mo behaves conservatively, whereas it normally enriches within organic matter and iron sulfides under anoxic conditions (Helz et al., 1996; Neubert et al., 2008; Algeo and Tribovillard, 2009). In anoxic conditions Mo is completely removed from seawater and accumulates in surface sediments (Neubert et al., 2008). Under oxic conditions U is present in its oxidized form U(VI) showing a conservative behavior (e.g., Hu et al., 2014), whereas in suboxic conditions (within the iron reduction zone) U(VI) is reduced to the insoluble U(IV). The uptake of insoluble U(IV) is facilitated by the presence of organic matter. The overall Mo/U ratio decreases in the iron reduction zone. Molybdenum content in all but two carbonate concretions (Cal-C and Cal-N) is consistently greater than the crustal average (1–2 ppm; Taylor and McLennan, 1985) and much higher than that expected for pure carbonate rocks (0.02 ppm; Neubert et al., 2008). The high Mo contents in calcite/aragonite (average 18.3 ppm), siderite (average 36.4 ppm) and sulfide (average 111.2 ppm) concretions point toward suboxic to anoxic conditions during carbonate precipitation.

Whether suboxic authigenic carbonates retain moderate Mo content (up to 25 ppm) and low $(Mo/U)_{EF}^{1}$ values, sediments precipitated in euxinic conditions yield a much greater Mo content (>60 ppm; Hu et al., 2014) and $(Mo/U)_{EF}$ values (Algeo and Tribovillard, 2009). Anomalously high Mo concentrations are believed to reflect the formation of iron sulfides after the production of hydrogen sulfide during AOM (Sato et al., 2012; Hu et al., 2014). Therefore, high $(Mo/U)_{EF}$ ratios and Mo enrichment are considered to evidence the precipitation in a sulfidic conditions (Hu et al., 2014). Sulfidic conditions vary with the seepage activity and AOM-derived hydrogen sulfide and may spread from the shallow sediments to the water column producing anomalously high Mo enrichment (Sato et al., 2012; Hu et al., 2014). The anomalously high concentration of Mo in Paola Ridge authigenic carbonates is produced at times of intense seepage. During periods of lower discharge downward migration of seawater oxidizes AOM-generated hydrogen sulfide. This implies that hydrogen sulfide is

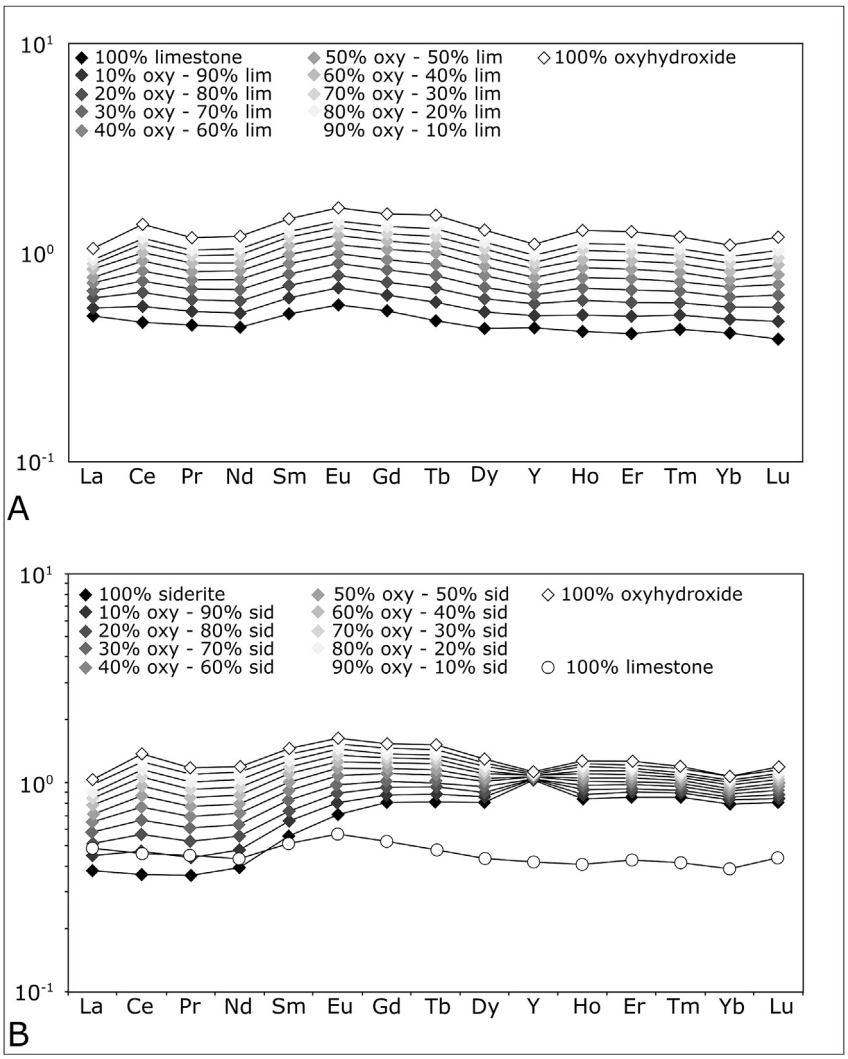

Fig. 11. A) Hypothetical mixing trend of average REE composition of calcite/aragonite and Fe-oxy-hydroxides. B) Hypothetical mixing trend of average REE composition of siderite (without sample Cal-MB4) and Fe-oxy-hydroxides.

maintained at a low level for Mo enrichment and Fe-sulfides formation. Whilst calcite/aragonite shows average $(Mo/U)_{EF}$ of 2.88, reflecting precipitation from sulfidic pore water, dolomite crusts show $(Mo/U)_{EF}$ values as low as 0.31 reflecting a much lower sulfide concentration (Algeo and Tribovillard, 2009; Hu et al., 2014) likely related to a lower methane flux. Siderite, on the other hand, yields higher $(Mo/U)_{EF}$ values (average 32.2), which are evidence of precipitation under strong anoxic conditions.

Varying $(Mo/U)_{EF}$, Ce anomalies and carbonate phases are better explained by temporary oxic conditions and variations in sulfide concentration induced by seepage flux changes (Feng et al., 2009; Birgel et al., 2011; Hu et al., 2014). These changes have probably been triggered by allogenic rapid changes in palaeoenvironmental and palaeoceanographic conditions (Rovere, unpublished data). It is important to note how calcite/aragonite and siderite concretions never co-occur, revealing a likely difference in the seepage conditions along R1MV and RMV, where ^{13}C-rich siderite occurs, and along the mud diapirs, where siderite is lacking but ^{13}C-poor AOM-related calcite/aragonite concretions are abundant.

6. Concluding remarks

Paola Ridge, along the NW Calabrian margin, is one of the few reported deep sea sites of precipitation of authigenic carbonates in the Tyrrhenian Sea. Authigenic mineral concretions were collected in near sub-bottom sediments along two alleged mud volcanoes (RMV and R1MV) and two diapirs (D1 and D2). A complete array of geochemical analyses has been performed to unravel the effects of discontinuous methane seepage on the genesis and early diagenesis of shallow sub-bottom sediments. Along the Paola Ridge the variable composition of the seeping fluids and the dynamic nature of the seepage induced fluctuation of the sulfate-methane transition zone (SMTZ) with consequent precipitation of diverse authigenic phases. The Paola Ridge sediments provide an unparalleled laboratory for testing the interaction between seeping fluids and different co-occurring authigenic minerals. Particularly siderite concretions, which abound in the study area, are rarely observed at seepage sites elsewhere in the Mediterranean Sea.

Negative $\delta^{13}C$ values together with the presence of chemosymbiotic bivalves are characteristic of a precipitation of calcite and aragonite within the AOM zone. Evidences of AOM are restricted to the D1 and D2 diapirs. Along D1 and D2 calcite/aragonite precipitate at time of moderate to high methane flux within the SMTZ close to the seafloor, under the influence of bottom seawater. Dolomite crusts precipitated at time of i) low methane flux (low sulfide concentrations) or ii) extremely vigorous methane seepage

(high sulfite concentrations). The low $(Mo/U)_{EF}$ ratio in the studied samples points toward the latter. This scenario of discontinuous seepage is corroborated by the REE distribution and trace elements concentration, and particularly by the lack of a Ce anomaly and the $(Mo/U)_{EF}$ ratio within the authigenic minerals.

RMV and R1MV sediments are rich in sulfide concretions and siderite. These structures (RMV and R1MV), previously described as mud volcanoes, where CO_2-rich gas venting is active at the seafloor, show ca. 6 m of highly deformed mud lacking any evidence of AOM. Along RMV and R1MV during periods of high flux the abundance of sulfate and Fe active ions fostered the precipitation of pyrite at the expenses of siderite. During periods of lower gas discharges the SMTZ deepens and the decreased sulfide concentration, associated with the increase of dissolved Fe^{2+}, facilitates the precipitation of siderite. Siderite precipitation occurred under prolonged anoxic conditions as shown by LREE fractionation and high $(Mo/U)_{EF}$. Most likely the precipitation of siderite took place within the methanogenic zone, as suggested by ^{13}C enrichment, and was affected by intense crustal CO_2 venting that induced sensible ^{18}O enrichment. The presence of intense ongoing CO_2-rich gas discharges, characterized by $\delta^{13}C\text{-}CO_2$ values slightly < -1‰ V-PDB, along RMV and R1MV structures and the Y/Ho chondritic ratios of the carbonates suggest the presence of a deep-seated source feeding these gas vents. The lack of consistent methane concentrations within the bottom sea water, coupled with lack of AOM precipitates, suggests that RMV and R1MV structures are not related to seepage of biogenic or thermogenic methane and cannot unambiguously be considered mud volcanoes.

The new data set sheds light into a complex seep-related scenario. Nevertheless the events can not be unambiguously constraint because of the lack of numerical and radiometric dating of the concretions. Future work focused on radiometric dating of the carbonate concretions may reveal, for instance, whether the deposition during a glacial age has been a major control factor for heavy oxygen enrichment. Moreover, although the presence of CO_2-rich gas suggests the presence of a deep-seated source of venting fluids, the carbon isotopic composition of the gases presented here is not unambiguously evidence for gas provenance. Further detail work on venting gas along Paola Ridge, through He isotopes characterization, may be resolutive in defining whether a mantle contribution was occurring during formation of the authigenic minerals. Further geophysical studies will also shed light on the geological processes that cause differences in fluid seepage between R1MV and RMV.

This paper shows that studies that combine trace elements and REE analysis have a great potential to shed light on the causes of both siderite precipitation and reconstruction of environmental conditions, which can lead to a variety of authigenic mineral precipitation and can be used to unravel fluid-rocks interaction active at other seepage sites.

Acknowledgements

Thanks are due to L. Giannini (Department of Earth Sciences, University of Florence) and E.M. Selmo (Department of Physics and Earth Sciences, University of Parma) for the gas sampling and the isotopic analyses of the carbonates, respectively. FF thanks T.O. Bineli Betsi and T. Kelepile (BIUST) for the precious advices concerning sulfides petrography. Thanks are due to Graeme Bremner (BIUST) for proofreading the early version of the manuscript. Two anonymous reviewers and the Editor N. Preto are gratefully acknowledged for their useful comments and suggestions that improved an early version of the manuscript.

This research was supported by the flagship project Ritmare (www.ritmare.it) funded by the Italian Ministry of Research and Education (MIUR).

Appendix A. Supplementary data

Supplementary data related to this article can be found at http://dx.doi.org/10.1016/j.marpetgeo.2017.05.031.

References

Al-Aasm, I.S., Taylor, B.E., South, B., 1990. Stable isotope analysis of multiple carbonate samples using selective acid extraction. Chem. Geol. 80, 119–125.
Algeo, T., Tribovillard, N., 2009. Environmental analysis of paleoceanographic systems based on molybdenum–uranium covariation. Chem. Geol. 268, 211–225.
Allwood, A.C., Kamber, B.S., Walter, M.R., Burch, I.W., Kanik, I., 2010. Trace elements record depositional history of an Early Archean stromatolitic carbonate platform. Chem. Geol. 270, 148–163.
Aloisi, G., Pierre, C., Rouchy, J.-M., Foucher, J.-P., Woodside, J., 2000. Methane-related authigenic carbonates of eastern Mediterranean Sea mud volcanoes and their possible relation to gas hydrate destabilisation. Earth Planet. Sci. Lett. 184, 321–338.
Angeletti, L., Canese, S., Franchi, F., Montagna, P., Reitner, J., Walliser, E.O., Taviani, M., 2015. The chimney forest of the deep Montenegrin margin, southeastern Adriatic Sea. Mar. Pet. Geol. 66, 542–554.
Bahrig, B., 1988. Palaeo-environment information from deep water siderite (Lake of Laach, West Germany). In: Fleet, A.J., et al. (Eds.), Lacustrine Petroleum Source Rocks, vol. 40. Geological Society of London Special Publication, pp. 153–158.
Bau, M., 1996. Controls on the fractionation of isovalent trace elements in magmatic and aqueous systems: evidence from Y/Ho, Zr/Hf, and lanthanide tetrad effect. Contrib. Mineral. Pet. 123, 323–333.
Bau, M., Dulski, P., 1996. Distribution of yttrium and rare-earth elements in the Penge and Kuruman iron-formations, transvaal supergroup, South Africa. Precambrian Res. 79, 37–55.
Bau, M., Dulski, P., 1999. Comparing yttrium and rare earths in hydrothermal fluids from the Mid-Atlantic Ridge: implications for Y and REE behaviour during near-vent mixing and for the Y/Ho ratio of Proterozoic seawater. Chem. Geol. 155, 77–90.
Bau, M., Koschinsky, A., 2009. Oxidative scavenging of cerium on hydrous Fe oxide: evidence from the distribution of rare earth elements and yttrium between Fe oxides and Mn oxides in hydrogenetic ferromanganese crusts. Geochem. J. 43, 37–47.
Bau, M., Koschinsky, A., Dulski, P., Hein, J.R., 1996. Comparison of the partitioning behaviours of yttrium, rare earth elements, and titanium between hydrogenetic marine ferromanganese crusts and seawater. Geochim. Cosmochim. Acta 60, 1709–1725.
Bau, M., Möller, P., Dulski, P., 1997. Yttrium and lanthanides in eastern Mediterranean seawater and their fractionation during redox-cycling. Mar. Chem. 56, 123–131.
Bayon, G., German, C.R., Burton, K.W., Nesbitt, R.W., Rogers, N., 2004. Sedimentary Fe–Mn oxy-hydroxides as paleoceanographic archives and the role of aeolian flux in regulating oceanic dissolved REE. Earth Planet. Sci. Lett. 224, 477–492.
Berner, R.A., 1981. A new geochemical classification of sedimentary environments. J. Sediment. Pet. 51, 359–365.
Birgel, D., Feng, D., Roberts, H.H., Peckmann, J., 2011. Changing redox conditions at cold seeps as revealed by authigenic carbonates from Alaminos Canyon, northern Gulf of Mexico. Chem. Geol. 285, 82–96.
Blumenberg, M., Walliser, E.O., Taviani, M., Seifert, R., Reitner, J., 2015. Authigenic carbonate formation and its impact on the biomarker inventory at hydrocarbon seeps – a case study from the Holocene Black Sea and the Plio-Pleistocene Northern Apennines (Italy). Mar. Pet. Geol. 66, 532–541.
Boetius, A., Suess, E., 2004. Hydrate Ridge: a natural laboratory for the study of microbial life fueled by methane from near-surface gas hydrates. Chem. Geol. 205, 291–310. http://dx.doi.org/10.1016/j.chemgeo.2003.12.034.
Boetius, A., Ravenschlag, K., Schubert, C.J., Rickert, D., Widdel, F., Gieseke, A., Amann, R., Jørgensen, B.B., Witte, U., Pfannkuche, O., 2000. A marine microbial consortium apparently mediating anaerobic oxidation of methane. Nature 407, 623–626.
Bohrmann, G., Greinert, J., Suess, E., Torres, M.E., 1998. Authigenic carbonates from the Cascadia subduction zone and their relation to gas hydrate stability. Geology 26, 647–650.
Byrne, R.H., Liu, X., Schijf, J., 1996. The influence of phosphate coprecipitation on rare earth element distributions in natural waters. Geochim. Cosmochim. Acta 60, 3341–3346.
Cabassi, J., Vaselli, O., Tassi, F., Giannini, L., 2011. Studio idrogeochimico delle acque sotterranee nella porzione settentrionale del Comune di Arezzo. Internal report; Department of Earth Sciences – University of Florence, Italy, p. 42 (In Italian).
Caliro, S., Chiodini, G., Moretti, R., Avino, R., Granieri, D., Russo, M., Fiebig, J., 2007. The origin of the fumaroles of La Solfatara (campi flegrei, south Italy). Geochim. Cosmochim. Acta 71, 3040–3055.
Campbell, K.A., Francis, D.A., Collins, M., Gregory, M.R., Nelson, C.S., Greinert, J., Aharon, P., 2008. Hydrocarbon seep-carbonates of a miocene forearc (East coast basin), north Island, New Zealand. Sediment. Geol. 204, 83–105.

Cangemi, M., Di Leonardo, R., Bellanca, A., Cundy, A., Neri, R., Angelone, M., 2010. Geochemistry and mineralogy of sediments and authigenic carbonates from the Malta Plateau, Strait of Sicily (Central Mediterranean): relationships with mud/fluid release from a mud volcano system. Chem. Geol. 276, 294–308. http://dx.doi.org/10.1016/j.chemgeo.2010.06.014.

Capozzi, R., Guido, F.L., Oppo, D., Gabbianelli, G., 2012. Methane-derived authigenic carbonates (MDAC) in northern-central Adriatic Sea: relationships between reservoir and methane seepages. Mar. Geol. 332–334, 174–188.

Carothers, W.W., Adami, L.H., Rosenbauer, R.J., 1988. Experimental oxygen isotope fractionation between siderite-water and phosphoric acid liberated CO_2-siderite. Geochim. Cosmochim. Acta 52, 2445–2450.

Cau, S., Franchi, F., Roveri, M., Taviani, M., 2015. The pliocene-age stirone river hydrocarbon chemoherm complex (northern apennines, Italy). Mar. Pet. Geol. 66, 582–595.

Cavalazzi, B., Agangi, A., Barbieri, R., Franchi, F., Gasparotto, G., 2014. The formation of low-temperature sedimentary pyrite and its relationship with biologically induced processes. Geol. Ore Depos. 56, 395–408.

Ceramicola, S., Praeg, D., Cova, A., Accettella, D., Zecchin, M., 2014. Seafloor distribution and last glacial to postglacial activity of mud volcanoes on the Calabrian accretionary prism, Ionian Sea. Geo-Marine Lett. 34, 111–129. http://dx.doi.org/10.1007/s00367-013-0354-y.

Chafetz, H.S., Buczynski, C., 1992. Bacterially induced lithification of microbial mats. Palaios 7, 277–293.

Chiodini, G., Marini, L., Russo, M., 2001. Geochemical evidence for the existence of high-temperature hydrothermal brines at Vesuvio volcano. Italy. Geochim. Cosmochim. Acta 65, 2129–2147.

Clayton, R.N., Epstein, S., 1961. The use of oxygen isotopes in high-temperature geological thermometry. J. Geol. 69, 447–452.

Cocker, J.D., Griffin, B.J., Muehlenbachs, K., 1982. Oxygen and carbon isotope evidence for seawater-hydrothermal alteration of Macquarie Island ophiolite. Earth Plan. Sci. Lett. 61, 112–122.

Corliss, J.B., Dymond, J., Gordon, L.I., Edmond, J.M., von Herzen, R.P., Ballard, R.D., Green, K., Williams, D., Bainbridge, A., Crane, K., van Andel, T.H., 1979. Submarine thermal springs on the Galápagos Rift. Science 203, 1073–1083.

CRC, 2005. Handbook of chemistry and Physics. In: Lide, David R. (Ed.), Section 14, Geophysics, Astronomy, and Acoustics; Abundance of Elements in the Earth's Crust and in the Sea, 85th Edition. 1CRC Press, Boca Raton, Florida.

Curtis, C.D., Coleman, M.L., 1986. Controls on the precipitation of early diagenetic calcite, dolomite, and siderite concretions in complex depositional sequences. In: Gautier, D.L. (Ed.), Roles of Organic Matter in Sediment Diagenesis, vol. 38. Society of Economic Paleontologists and Mineralogists Special Publication, pp. 23–33.

Curtis, C.D., Petrowski, C., Ortel, G., 1972. Stable carbon isotope ratios within carbonate concretions: a clue to place and time of formation. Nature 235, 98–100.

Dählmann, A., de Lange, G.J., 2003. Fluid–sediment interactions at Eastern Mediterranean mud volcanoes: a stable isotope study from ODP Leg 160. Earth Planet. Sci. Lett. 212, 377–391.

Dalla Valle, G., Gamberi, F., 2011. Pockmarks and seafloor instability in the Olbia continental slope (northeastern Sardinian margin, Tyrrhenian Sea). Mar. Geophys. Res. 32, 193–205.

Elderfield, H., Greaves, M.J., 1982. The rare earth elements in seawater. Nature 296, 214–219.

Elderfield, H., Upstill-Goddard, R., Sholkovitz, E.R., 1990. The rare earth elements in rivers, estuaries and coastal sea waters: processes affecting crustal input of elements to the ocean and their significance to the composition of sea water. Geochim. Cosmochim. Acta 54, 971–991.

Faccenna, C., Molin, P., Orecchio, B., Olivetti, V., Bellier, O., Funiciello, F., Minelli, L., Piromallo, C., Billi, A., 2011. Topography of the Calabria subduction zone (southern Italy): clues for the origin of Mt. Etna. Tectonics 30, TC1003.

Feng, D., Chen, D., Peckmann, J., 2009. Rare earth elements in seep carbonates as tracers of variable redox conditions at ancient hydrocarbon seeps. Terra Nova 21, 49–56.

Fernandez, A., van Dijk, J., Müller, I.A., Bernasconi, S.M., 2016. Siderite acid fractionation factors for sealed and open vessel digestions at 70°C and 100°C. Chem. Geol. 444, 180–186.

Franchi, F., Hofmann, A., Cavalazzi, B., Wilson, A., Barbieri, R., 2015. Differentiating marine vs hydrothermal processes in Devonian carbonate mounds using rare earth elements (Kess Kess mounds, Anti-Atlas, Morocco). Chem. Geol. 409, 69–86.

Franchi, F., Turetta, C., Cavalazzi, B., Corami, F., Barbieri, R., 2016. Trace elements and REE geochemistry of middle devonian carbonate mounds (maïder basin, eastern anti-atlas, Morocco): implications for early diagenetic processes. Sed. Geol. 343, 56–71.

Fritz, P., Binda, P.L., Folinsbee, F.E., Krouse, H.R., 1971. Isotopic composition of diagenetic siderites from Cretaceous sediments in Western Canada. J. Sediment. Pet. 41, 282–288.

Gamberi, F., Rovere, M., 2010. Mud diapirs, mud volcanoes and fluid flowing: the rear of the Calabrian Arc Orogenic Wedge (southeastern Tyrrhenian Sea). Basin Res. 22, 452–464.

Geletti, R., Del Ben, A., Busetti, M., Ramella, R., Volpi, V., 2008. Gas seeps linked to salt structures in the central Adriatic Sea. Basin Res. 20, 473–487. http://dx.doi.org/10.1111/j.1365-2117.2008.00373.x.

German, C.R., Elderfield, H., 1990. Application of the Ce anomaly as a paleoredox indicator: the ground rules. Paleoceanography 5, 823–833.

Goldstein, S.J., Jacobsen, S.B., 1988. Rare earth elements in river waters. Earth Planet. Sci. Lett. 89, 35–47.

Gutscher, M.-A., Dominguez, S., de Lepinay, B.M., Pinheiro, L., Gallais, F., Babonneau, N., Cattaneo, A., Le Faou, Y., Barreca, G., Micallef, A., Rovere, M., 2015. Tectonic expression of an active slab tear from high-resolution seismic and bathymetric data offshore Sicily (Ionian Sea). Tectonics 34. http://dx.doi.org/10.1002/2015TC003898.

Haley, B.A., Klinkhammer, G.P., McManus, J., 2004. Rare earth elements in pore waters of marine sediments. Geochim. Cosmochim. Acta 68, 1265–1279.

Hein, J.R., Normark, W.R., McIntyre, B.R., Lorenson, T.D., Powell II, C.L., 2006. Methanogenic calcite, ^{13}C-depleted bivalve shells, and gas hydrate from a mud volcano offshore southern California. Geology 34, 109–112.

Helz, G.R., Miller, C.V., Charnock, J.M., Mosselmans, J.F.W., Pattrick, R.A.D., Garner, C.D., Vaughan, D.J., 1996. Mechanism of molybdenum removal from the sea and its concentration in black shales: EXAFS evidence. Geochim. Cosmochim. Acta 60, 3631–3642.

Hicks, K.S., Compton, J.S., McCracken, S., Vecsei, A., 1996. Origin of diagenetic carbonate minerals recovered from the New Jersey continental slope. In: Mountain, G.S., Miller, K.G., Blum, P., Poag, C.W., Twichell, D.C. (Eds.), Proc. ODP, Sci. Results, vol. 150. TX (Ocean Drilling Program), College Station, pp. 311–323.

Himmler, T., Bach, W., Bohrmann, G., Peckmann, J., 2010. Rare earth elements in authigenic methane-seep carbonates as tracers for fluid composition during early diagenesis. Chem. Geol. 277, 126–136.

Hovland, M., Gardner, J.V., Judd, A.G., 2002. The significance of pockmarks to understanding fluid flow processes and geohazards. Geofluids 2, 127–136. http://dx.doi.org/10.1046/j.1468-8123.2002.00028.x.

Hu, Y., Feng, D., Peckmann, J., Roberts, H.H., Chen, D., 2014. New insights into cerium anomalies and mechanisms of trace metal enrichment in authigenic carbonate from hydrocarbon seeps. Chem. Geol. 381, 55–66.

Irwin, H., Curtis, C.D., Coleman, M., 1977. Isotopic evidence for source of diagenetic carbonates formed during burial of organic-rich sediments. Nature 269, 209–213.

Jimenez-Lopez, C., Romanek, C.S., 2004. Precipitation kinetics and carbon isotope partitioning of inorganic siderite at 25°C and 1 atm. Geochim. Cosmochim. Acta 68, 557–571.

Joseph, A., 2017. Chapter 6-seafloor hot chimneys and cold seeps: mysterious life around them. Investigating Seafloors Oceans 307–375.

Kamber, B.S., Bolhar, R., Webb, G.E., 2004. Geochemistry of late Archaean stromatolites from Zimbabwe; evidence for microbial life in restricted epicontinental seas. Precambrian Res. 132, 379–399.

Kim, S.-T., O'Neil, J.R., 1997. Equilibrium and nonequilibrium oxygen isotope effects in synthetic carbonates. Geochim. Cosmochim. Acta 61, 3461–3475.

Kim, S.-T., O'Neil, J.R., Hillaire-Marcel, C., Mucci, A., 2007. Oxygen isotope fractionation between synthetic aragonite and water: influence of temperature and Mg^{2+} concentration. Geochim. Cosmochim. Acta 71, 4704–4715.

Kim, J.-H., Torres, M.E., Haley, B.A., Kastner, M., Pohlman, J.W., Riedel, M., Lee, Y.-J., 2012. The effect of diagenesis and fluidmigration on rare earth element distribution in pore fluids of the northern Cascadia accretionary margin. Chem. Geol. 291, 152–165.

Klinkhammer, G.P., Elderfield, H., Edmond, J.M., Mitra, A., 1994. Geochemical implications of rare earth element patterns in hydrothermal fluids from mid-ocean ridges. Geochim. Cosmochim. Acta 58, 5105–5113.

Krastel, S., Spiess, V., Ivanov, M., Weinrebe, W., Bohrmann, G., Shashkin, P., Heidersdorf, F., 2003. Acoustic investigations of mud volcanoes in the sorokin trough, black sea. Geo-Marine Lett. 23, 230–238. http://dx.doi.org/10.1007/s00367-003-0143-0.

Lawrence, M.G., Greig, A., Collerson, K.D., Kamber, B.S., 2006. Rare earth element and yttrium variability in south East queensland waterways. Aquat. Geochem 12, 39–72.

Lécuyer, C., Fourcade, S., 1991. Oxygen isotope evidence for multi-stage hydrothermal alteration at a fossil slow-spreading center: the Silurian Trinity ophiolite (California, U.S.A.). Chem. Geol. 87, 231–246.

Lécuyer, C., Allemand, P., 1999. Modelling of the oxygen isotope evolution of seawater: implications for the climate interpretation of the $\delta^{18}O$ of marine sediments. Geochim. Cosmochim. Acta 63, 351–361.

Levin, L.A., Mendoza, G.F., Grupe, B.M., 2016. Methane seepage effects on biodiversity and biological traits of macrofauna inhabiting authigenic carbonates. Deep Sea Res. Part II Top. Stud. Oceanogr. 1–16. http://dx.doi.org/10.1016/j.dsr2.2016.05.021.

Lietard, C., Pierre, C., 2009. Isotopic signatures ($\delta^{18}O$ and $\delta^{13}C$) of bivalve shells from cold seeps and hydrothermal vents. Geobios 42, 209–219.

Løseth, H., Gading, M., Wensaas, L., 2009. Hydrocarbon leakage interpreted on seismic data. Mar. Pet. Geol. 26, 1304–1319. http://dx.doi.org/10.1016/j.marpetgeo.2008.09.008.

Lykousis, V., Alexandri, S., Woodside, J., de Lange, G., Dählmann, A., Perissoratis, C., Heeschen, K., Ioakim, Chr., Sakellariou, D., Nomikou, P., Rousakis, G., Casas, D., Ballas, D., Ercilla, G., 2009. Mud volcanoes and gas hydrates in the Anaximander mountains (Eastern Mediterranean Sea). Mar. Pet. Geol. 26, 854–872.

Maekawa, T., 2004. Experimental study on isotopic fractionation in water during gas hydrate formation. Geochem. J. 38, 129–138.

Magalhães, V.H., Pinheiro, L.M., Ivanov, M.K., Kozlova, E., Blinova, V., Kolganova, J., Vasconcelos, C., McKenzie, J.A., Bernasconi, S.M., Kopf, A.J., Díaz-del-Río, V., González, F.J., Somoza, L., 2012. Formation processes of methane-derived authigenic carbonates from the Gulf of Cadiz. Sediment. Geol. 243–244, 155–168.

Mascle, J., Mary, F., Praeg, D., Brosolo, L., Camera, L., Ceramicola, S., Dupré, S., 2014.

Distribution and geological control of mud volcanoes and other fluid/free gas seepage features in the Mediterranean Sea and nearby Gulf of Cadiz. Geo-Mar. Lett. 34, 89–110. http://dx.doi.org/10.1007/s00367-014-0356-4.
Matsumoto, R., 1989. Isotopically heavy oxygen-containing siderite derived from the decomposition of methane hydrate. Geology 17, 707–710.
Mazzini, A., Aloisi, G., Akhmanov, G.G., Parnell, J., Cronin, B.T., Murphy, P., 2005. Integrated petrographic and geochemical record of hydrocarbon seepage on the Vøring Plateau. J. Geol. Soc. Lond 162, 815–827.
Micallef, A., Berndt, C., Debono, G., 2011. Fluid flow systems of the Malta plateau, central mediterranean sea. Mar. Geol. 284, 74–85. http://dx.doi.org/10.1016/j.margeo.2011.03.009.
Michard, A., 1989. Rare earth element systematics in hydrothermal fluids. Geochim. Cosmochim. Acta 53, 745–750.
Milia, A., Turco, E., Pierantoni, P.P., Schettino, A., 2009. Four-dimensional tectono-nostratigraphic evolution of the Southeastern peri-Tyrrhenian basins (margin of Calabria, Italy). Tectonophysics 476, 41–56.
Minissale, A., Magro, G., Vaselli, O., Verrucchi, C., Perticone, I., 1997. Geochemistry of water and gas discharges from the Mt. Amiata silicic complex and surrounding areas (central Italy). J. Vulcanol. Geotherm. Res. 79, 223–251.
Monty, C.L.V., 1995. The rise and nature of carbonate mudmounds: an introductory actualistic approach. In: Monty, C.L.V., Bosence, D.W.J., Bridges, P.H., Pratt, B.R. (Eds.), Carbonate Mud-Mounds, Their Origin and Evolution, vol. 23. Spec. Publ. Int. Assoc. Sedimentol., Blackwell, Oxford, pp. 11–48.
Mozley, P.S., Wersin, P., 1992. Isotopic composition of siderite as an indicator of depositional environment. Geology 20, 817–820.
Muehlenbachs, K., Hodges, F.N., 1978. Oxygen isotope geochemistry of rocks from DSDP LEG 46. Reps. DSDP 46, 257–259.
Murray, R.W., Buchholtz ten Brink, M.R., Gerlach, D.C., Price Russ III, G., Jones, D.L., 1991. Rare earth, major, and trace elements in chert from the Franciscan Complex and Monterey Group, California: assessing sources to fine-grained marine sediments. Geochim. Cosmochim. Acta 55, 1875–1895.
Neubert, N., Nagler, T.F., Böettcher, M.E., 2008. Sulfidity controls molybdenum isotope fractionation into euxinic sediments: evidence from the modern Black Sea. Geology 36, 775–778.
Nothdurft, L.D., Webb, G.E., Kamber, B.S., 2004. Rare earth element geochemistry of Late Devonian reefal carbonates, Canning Basin, Western Australia: confirmation of a seawater REE proxy in ancient limestones. Geochim. Cosmochim. Acta 68, 263–283.
Nozaki, Y., Zhang, J., Amakawa, H., 1997. The fractionation between Y and Ho in the marine environment. Earth Planet. Sci. Lett. 148, 329–340.
Olivier, N., Boyet, M., 2006. Rare earth and trace elements of microbialites in Upper Jurassic coral- and sponge-microbialite reefs. Chem. Geol. 230, 105–123.
Pack, A., Russell, S.S., Michael, J., Shelley, G., van Zuilen, M., 2007. Geo- and cosmochemistry of the twin elements yttrium and holmium. Geochim. Cosmochim. Acta 71, 4592–4608.
Paonita, A., Favara, R., Nuccio, P.M., Sortino, F., 2002. Genesis of fumarolic emissions as inferred by isotope mass balances: CO_2 and water at Vulcano Island, Italy. Geochim. Cosmochim. Acta 66, 759–772.
Passaro, S., Tamburrino, S., Vallefuoco, M., Tassi, F., Vaselli, O., Giannini, L., Chiodini, L., Caliro, S., Sacchi, M., Rizzo, A.L., Ventura, G., 2016. Seafloor doming driven by degassing processes unveils sprouting volcanism in coastal areas. Sci. Rep. 6, 22448. http://dx.doi.org/10.1038/srep22448.
Paull, C.K., Hecker, B., Commeau, R., Freeman-Lynde, R.P., Neumann, C., Corso, W.P., Golubic, S., Hook, J.E., Sikes, E., Curray, J.T., 1984. The first Biological communities at the Florida escarpment resemble hydrothermal vent taxa. Science 226, 965–967.
Peckmann, J., Reimer, A., Luth, U., Luth, C., Hansen, B.T., Heinicke, C., Hoefs, J., Reitner, J., 2001. Methane-derived carbonates and authigenic pyrite from the northwestern Black Sea. Mar. Geol. 177, 129–150.
Peckmann, J., Birgel, D., Kiel, S., 2009. Molecular fossils reveal fluid composition and flow intensity at a Cretaceous seep. Geology 37, 847–850.
Peckmann, J., Thiel, V., 2004. Carbon cycling at ancient methane-seeps. Chem. Geol. 205, 443–467.
Peters, M., Strauss, H., Petersen, S., Kummer, N.A., Thomazo, C., 2011. Hydrothermalism in the Tyrrhenian Sea: inorganic and microbial sulfur cycling as revealed by geochemical and multiple sulfur isotope data. Chem. Geol. 280, 217–231. http://dx.doi.org/10.1016/j.chemgeo.2010.11.011.
Pourret, O., Davranche, M., Gruau, G., Dia, A., 2008. New insights into cerium anomalies in organic-rich alkaline waters. Chem. Geol. 251, 120–127.
Reynard, B., Lécuyer, C., Grandjeau, P., 1999. Crystal-chemical controls on rare earth element concentrations in fossil biogenic apatite and implications for paleoenvironmental reconstructions. Chem. Geol. 155, 233–242.
Rongemaille, E., Bayon, G., Pierre, C., Bollinger, C., Chu, N.C., Fouquet, Y., Riboulot, V., Voisset, M., 2011. Rare earth elements in cold seep carbonates from the Niger delta. Chem. Geol. 286, 196–206.
Rovere, M., Gamberi, F., Mercorella, A., Rashed, H., Gallerani, A., Leidi, E., Marani, M., Funari, V., Pini, G.A., 2014. Venting and seepage systems associated with mud volcanoes and mud diapirs in the southern Tyrrhenian Sea. Mar. Geol. 347, 153–171.
Rovere, M., Rashed, H., Pecchioni, E., Mercorella, A., Ceregato, A., Leidi, E., Gamberi, F., Vaselli, O., 2015. Habitat mapping of cold seeps associated with authigenic mineralization (Paola Ridge, southern Tyrrhenian Sea): combining seafloor backscatter with biogeochemistry signals. Ital. J. Geosci. 134, 23–31.
Sato, H., Hayashi, K.-i., Ogawa, Y., Kawamura, K., 2012. Geochemistry of deep sea sediments at cold seep sites in the Nankai Trough: insights into the effect of anaerobic oxidation of methane. Mar. Geol. 323–325, 47–55.
Savini, A., Malinverno, E., Etiope, G., Tessarolo, C., Corselli, C., 2009. Shallow seep-related seafloor features along the Malta plateau (Sicily channel – Mediterranean Sea): morphologies and geo-environmental control of their distribution. Mar. Pet. Geol. 26, 1831–1848. http://dx.doi.org/10.1016/j.marpetgeo.2009.04.003.
Schneider von Deimling, J., Linke, P., Schmidt, M., Rehder, G., 2015. Ongoing methane discharge at well site 22/4b (NorthSea) and discovery of a spiral vortex bubble plume motion. J. Mar. Pet. Geol. 68, 618–630.
Solomon, E.A., Kastner, M., Jannasch, H., Robertson, G., Weinstein, Y., 2008. Dynamic fluid flow and chemical fluxes associatedwith a seafloor gas hydrate deposit on the northern Gulf of Mexico slope. Earth Planet. Sci. Lett. 270, 95–105.
Sommer, S., Schmidt, M., Linke, P., 2015. Continuous inline mapping of a dissolved methane plume at a blowout site in the Central North Sea UK using a membrane inlet mass spectrometer–Water column stratification impedes immediate methane release into the atmosphere. J. Mar. Pet. Geol. 68, 766–775.
Sultan, N., Bohrmann, G., Ruffine, L., Pape, T., Riboulot, V., Colliat, J.-L., Prunelé, A., De Dennielou, B., Garziglia, S., Himmler, T., Marsset, T., Peters, C.A., Rabiu, A., Wei, J., 2014. Pockmark formation and evolution in deep water Nigeria: rapid hydrate growth versus slow hydrate dissolution. J. Geophys. Res. Solid Earth 119, 2679–2694. http://dx.doi.org/10.1029/2010JB007453.
Taviani, M., 2001. Fluid venting and associated processes. In: Vai, G.B., Maltini, I.P. (Eds.), Anatomy of an Orogen: the Apennines and Adjacent Mediterranean Basins. Kluwer Academic Publisher, Great Britain, pp. 351–366.
Taviani, M., Angeletti, L., Ceregato, A., Foglini, F., Froglia, C., Trincardi, F., 2013. The Gela Basin pockmark field in the strait of Sicily (Mediterranean Sea): chemosymbiotic faunal and carbonate signatures of postglacial to modern cold seepage. Biogeosciences 10, 1–19.
Taviani, M., Franchi, F., Angeletti, L., Correggiari, A., López Correa, M., Maselli, V., Mazzoli, C., Peckmann, J., 2015. Biodetrital carbonates on the Adriatic continental shelf imprinted by oxidation of seeping hydrocarbons. J. Mar. Pet. Geol. 66, 511–531.
Taylor, S.R., McLennan, S.M., 1985. The Continental Crust: its Composition and Evolution. Blackwell Scientific Pub, Palo Alto, CA, 328 pp.
Taylor, K.G., Curtis, C.D., 1995. Stability and facies association of early diagenetic mineral assemblages: an example from a Jurassic ironstone- mudstone succession, UK. J. Sediment. Pet. 65, 358–368.
Tostevin, R., Shields, G.A., Tarbuck, G.M., He, T., Clarkson, M.O., Wood, R.A., 2016. Effective use of cerium anomalies as a redox proxy in carbonate-dominated marine settings. Chem. Geol. 438, 146–162.
Vasconcelos, C., McKenzie, J.A., Warthmann, R., Bernasconi, S.M., 2005. Calibration of the δ18O paleothermometer for dolomite precipitated in microbial cultures and natural environments. Geology 33, 317–320.
Vaselli, O., Tassi, F., Montegrossi, G., Capaccioni, B., Giannini, L., 2006. Sampling and analysis of fumarolic gases. Acta Vulcanol. 1–2, 65–76.
Vaselli, O., Tassi, F., Tedesco, D., Poreda, J.R., Caprai, A., 2011. Submarine and inland gas discharges from the campi flegrei (southern Italy) and the pozzuoli bay: geochemical clues for a common hydrothermal-magmatic source. Special volume on "research in shallow marine and fresh water systems". Procedia Earth Planet. Sci. 4, 57–73.
Vergnaud-Grazzini, C., 1971. ^{18}O changes in foraminiferal carbonates during the last 105 years in the Mediterranean Sea. Mar. Geol. 11, 261–282.
Viola, I., Oppo, D., Franchi, F., Capozzi, R., Dinelli, E., Liverani, B., Taviani, M., 2015. Mineralogy, geochemistry and petrography of methane-derived authigenic carbonates from Enza River, Northern Apennines (Italy). Mar. Pet. Geol. 66, 566–581.
Webb, G.E., Kamber, B.S., 2000. Rare earth elements in Holocene reefal microbialites: a new shallow seawater proxy. Geochim. Cosmochim. Acta 64, 1557–1565.
Whiticar, M.J., 1999. Carbon and hydrogen isotope systematics of bacterial formation and oxidation of methane. Chem. Geol. 161, 291–314.
Wittkop, C., Teranes, J., Lubenow, B., Dean, W.E., 2014. Carbon- and oxygen-stable isotopic signatures of methanogenesis, temperature, and water column stratification in Holocene siderite varves. Chem. Geol. 389, 153–166.
Zhang, J., Nozaki, Y., 1996. Rare earth elements and yttrium in seawater: ICP-MS determinations in the east caroline, coral sea, and south Fiji basins of the western south pacific ocean. Geochim. Cosmochim. Acta 60, 4631–4644.
Zhang, J., Nozaki, Y., 1998. Behavior of rare earth elements in seawater at the ocean margin: a study along the slopes of the Sagami and Nankai troughs near Japan. Geochim. Cosmochim. Acta 62, 1307–1317.
Zhang, J., Amakawa, H., Nozaki, Y., 1994. The comparative behaviors of yttrium and lanthanides in seawater of the North Pacific. Geophys. Res. Lett. 21, 2677–2680.
Zhang, F., Xu, H., Konishi, H., Kemp, J.M., Roden, E.E., Shen, Z., 2012. Dissolved sulfide-catalyzed precipitation of disordered dolomite: implications for the formation mechanism of sedimentary dolomite. Geochim. Cosmochim. Acta 97, 148–165.
Zhang, K., Zhu, X.-K., Yan, B., 2015. A refined dissolution method for rare earth element studies of bulk carbonate rocks. Chem. Geol. 412, 82–91.
Zhong, S., Mucci, A., 1995. Partitioning or rare earth elements (REEs) between calcite and seawater solutions at 25°C and 1 atm, and high dissolved REE concentrations. Geochim. Cosmochim. Acta 59, 443–453.